# Recent Advances in Niobium-Based Materials for Photocatalytic Solar Fuel Production

**Barbara Nascimento Nunes** [1,2] , **Osmando Ferreira Lopes** [2] , **Antonio Otavio T. Patrocinio** [2,*] and **Detlef W. Bahnemann** [1,3,*]

1   Institute of Technical Chemistry, Leibniz University Hannover, 30167 Hannover, Germany;
    nunes@iftc.uni-hannover.de
2   Laboratory of Photochemistry and Materials Science, Institute of Chemistry, Federal University of
    Uberlandia, Uberlandia 38400-902, Brazil; osmando@ufu.br
3   Laboratory 'Photoactive Nanocomposite Materials', Saint-Petersburg State University,
    Saint-Petersburg 199034, Russia
*   Correspondence: otaviopatrocinio@ufu.br (A.O.T.P.); bahnemann@iftc.uni-hannover.de (D.W.B.)

check for updates

**Abstract:** The search for renewable and clean energy sources is a key aspect for sustainable development as energy consumption has continuously increased over the years concomitantly with environmental concerns caused by the use of fossil fuels. Semiconductor materials have great potential for acting as photocatalysts for solar fuel production, a potential energy source able to solve both energy and environmental concerns. Among the studied semiconductor materials, those based on niobium pentacation are still shallowly explored, although the number of publications and patents on Nb(V)-based photocatalysts has increased in the last years. A large variety of Nb(V)-based materials exhibit suitable electronic/morphological properties for light-driving reactions. Not only the extensive group of $Nb_2O_5$ polymorphs is explored, but also many types of layered niobates, mixed oxides, and Nb(V)-doped semiconductors. Therefore, the aim of this manuscript is to provide a review of the latest developments of niobium based photocatalysts for energy conversion into fuels, more specifically, $CO_2$ reduction to hydrocarbons or $H_2$ eVolution from water. Additionally, the main strategies for improving the photocatalytic performance of niobium-based materials are discussed.

**Keywords:** niobium; water splitting; artificial photosynthesis; $Nb_2O_5$; niobates

## 1. Introduction

Increasing energy demand concomitantly with global warming is a major world concern. Currently, fuels and electricity supplies are still strongly dependent on nonrenewable sources. For instance, in 2018, the worldwide consumption of fossil energy was almost 36.5 billion barrels of oil, 3850 billion cubic meters of natural gas, and 3800 million tons oil equivalent of coal per year. As a consequence, more than 33,000 million tons of carbon dioxide was emitted, which represents an annual increasing of 2.0%, the fastest growth for seven years [1]. This scenario can trigger serious problems for the current and next generations such as the insufficiency of fossil fuel resources, air pollution, and also climate changes as a result of the greenhouse effect [2].

In the face of this issue, the development of methods to obtain energy in a clean and sustainable way becomes imperative. Therefore, solar light as a primary energy resource stands out for its advantages in terms of spread availability and accessibility in an inexhaustible and inexpensive way around the world. In addition, obtaining energy from the sun may cause less damage to the environment in relation to waste production, polluting gases emission, or impacts to different ecosystems. The possibility to convert light into valuable solar fuels from water or eVen $CO_2$ is a promising approach to provide clean

energy and, at the same time, contribute to diminishing the global warming effect [3]. Additionally, the total sum of renewable energy from all the reserves is around 1% of the solar energy supplied to the earth surface by the sun, that is, 173,000 TW. This amount of energy is more than 9000 times larger than the current total energy consumption of the world (17.91 TW in 2017). The challenge lies on the development of economically viable technologies for solar energy harvesting, storage, and utilization [4].

Thus, since Fujishima and Honda [5] reported the possibility of promoting the photo-oxidation of water on the surface of $TiO_2$ photoanodes, semiconductor materials have been extensively investigated as photocatalysts to store solar energy in chemical bonds. Among different photocatalysts, it is worth pointing out Nb(V)-based materials that have been investigated owing to their suitable electronic and morphological properties for light-driving reactions. Nb(V) is characterized by its high affinity to oxygen and its oxides exhibit different properties depending on the preparation and desired application [6,7]. Niobium pentoxide is considered the most thermodynamically stable Nb-based compound with more than 15 different structural configurations. Depending on the crystalline phase, its band-gap energy can vary from 3.2 eV to larger values such as 5 eV [8–10].

Besides $Nb_2O_5$ polymorphs, Nb(V) can also combine with oxygen to form extended lamellar structures resulting in polyoxy anions, the niobates. They are basically constituted of stacked negative charged layers with intercalated cations [11]. This configuration provides a considerable surface area and allows easy modification either by intercalation, superficial modification, or formation of nanosheets and nanoscrolls [12–14]. Furthermore, Nb(V) is also frequently applied as a doping agent. It is commonly combined to $TiO_2$ and considered one of the most promising dopants for modifying the matrix crystalline structure and minimize the electron–hole recombination [15–18].

In this paper, the recent developments of niobium-based materials for photocatalytic solar fuel production, especially those in the last three years, are systematically reviewed. The main strategies for improving the photocatalytic performance for $H_2$ production from water splitting and $CO_2$ reduction to hydrocarbons, focused on niobium species, will be presented. In Section 2, application to $H_2$ eVolution is discussed, followed by Section 3 related to $CO_2$ reduction.

## 2. H$_2$ eVolution and Water Splitting

### 2.1. Niobium Pentoxide (Nb$_2$O$_5$)

$Nb_2O_5$ is a typical *n*-type semiconductor that, along with other oxides, has been widely studied as a photocatalyst thanks to its electronic properties such as excellent chemical and thermal stability, large abundance, rich morphologies, and several polymorphs [19–22]. It is a white solid powder, insoluble in water, and can be dissolved just by fusion with strong basic or acid fluxes. In general, its structure is formed by $NbO_6$ octahedral, which can result in an amorphous state or may crystallize in a wide range of polymorphs with different physical properties [6,8]. Some of those polymorphs are pseudohexagonal (TT-$Nb_2O_5$), orthorhombic (T-$Nb_2O_5$), and monoclinic (B, H, R, and N-$Nb_2O_5$) [19]. The most known nomenclature is based on Brauer's system, in which the crystalline phases are identified by letters corresponding to the temperature at which they are obtained [8].

Despite these properties, bulk $Nb_2O_5$ is not able to achieve a considerable photoactivity owing to its low specific surface area and fast recombination rate of the photogenerated charge carriers [21]. In this sense, several approaches have been applied to increase its photocatalytic performance. One of them is to control the shape and morphology of particles in order to tune the $Nb_2O_5$ properties. This can be possible, for instance, by selecting a suitable precursor to obtain the desired configuration of $Nb_2O_5$. Wen and coauthors firstly synthesized orthorhombic $Nb_2O_5$ (O-$Nb_2O_5$) by a hydrothermal reaction using $K_4Nb_6O_{17}$ $4.5H_2O$ as a precursor. This sample exhibited rectangle nanosheets with a dominantly exposed (010) plane (Figure 1a–d) [22]. After acid treatment of $K_4Nb_6O_{17}$ $4.5H_2O$ to get $H_4Nb_6O_{17}$ $3H_2O$, the ion-exchanged material was treated hydrothermally for 24 h at different conditions of temperature (195–215 °C) and pH (1.5–11.5), as shown in Figure 1e. At first, by changing

the temperature at pH 3.5, X ray diffraction (XRD) results showed that the O-Nb$_2$O$_5$ phase began to be formed at 200 °C, and at 210 °C, the peaks of H$_4$Nb$_6$O$_{17}$ 3H$_2$O disappeared completely and all observed peaks could be indexed as the O-Nb$_2$O$_5$ phase. From the Figure 1e, it can be also observed that the O-Nb$_2$O$_5$ was obtained in all selected pHs; however, the authors reported that, at pH 3.5, the material showed higher crystallinity and more regular morphology. A commercial O-Nb$_2$O$_5$ sample with spherical morphology was used for comparison and exhibited a band gap value of 3.2 eV, in contrast to 3.0 eV for the as synthesized O-Nb$_2$O$_5$ rectangle nanosheets. Then, the photoelectrochemical activity of both samples was eValuated by measuring the photocurrent resulted from H$_2$ eVolution under 370 nm UV light irradiation (30 W·m$^{-2}$). Both photoelectrodes show very low dark current, but under illumination, the O-Nb$_2$O$_5$ nanosheet-based photoelectrode exhibited photocurrents 4.3 times higher than the commercial sample. The authors could justify the improved performance to a larger number of charge carriers coming from the exposed (010) facet with lower band gap energy, fewer recombination centers, and also faster charge transfer by the regular rectangle nanosheets with high crystallinity.
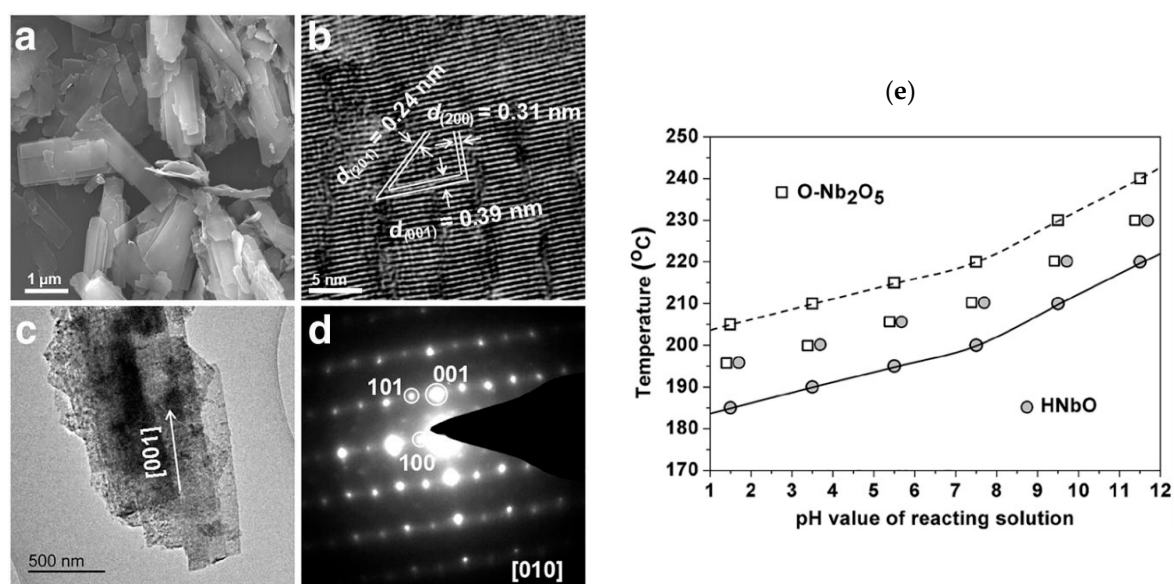


**Figure 1.** O-Nb$_2$O$_5$ microscopies images of (**a**) field emission scanning electron microscopy (FE-SEM), (**b**) high-resolution transmission electron microscopy (HRTEM), (**c**) transmission electron microscopy (TEM), and (**d**) selected area electron diffraction (SAED) pattern and (**e**) diagram for the transformation of O-Nb$_2$O$_5$ nanosheets from H$_4$Nb$_6$O$_{17}$ 3H$_2$O (HNbO) nanosheets under hydrothermal conditions. Reproduced with permission from the authors of [22]. Copyright (2019), Elsevier, Amsterdam, Netherlands.

Later, the same strategy was employed by the same group to obtain crystalline hexagonal Nb$_2$O$_5$ (H-Nb$_2$O$_5$) nanobelt clusters with an exposed (−110) plane [23]. In this case, a fiber-like K$_2$Nb$_2$O$_6$·H$_2$O material was used as precursor. In order to improve the photocatalytic performance of H-Nb$_2$O$_5$ under visible light, metallic Ag was deposited by in situ photoreduction. UV/vis diffuse reflectance spectra showed that the absorption edges were 375 nm for the H-Nb$_2$O$_5$ nanobelt clusters and 423 nm for the Ag-modified sample. Then, both samples were eValuated photoelectrochemically under simulated sunlight illumination (100 W m$^{-2}$) at zero applied voltage. The Ag-modified sample achieved a photocurrent of 10.73 μA, 535 times higher than that observed for bare H-Nb$_2$O$_5$, which was attributed to the improved light-harvesting efficiency as well as the better charge transfer performance.

Zhou and coauthors reported monoclinic Nb$_2$O$_5$ nanorod superstructures by a similar route using Sn$_2$Nb$_2$O$_7$ nanoparticles as the precursor [24]. SEM images showed that Nb$_2$O$_5$ nanorods were obtained with lengths around 2 μm and diameters of 200 nm. The light absorption properties

of the $Nb_2O_5$ nanorods were compared to those of commercial $Nb_2O_5$ powders and a considerable blue shift was observed in the absorption edge, which could be related to the nanosize of the former. Photocatalytic $H_2$ production was also eValuated with 0.5 wt% Pt as co-catalyst in 25% methanol aqueous solution, employing a 500 W high-pressure mercury lamp as light source. The $Nb_2O_5$ nanorod superstructures sample showed a $H_2$ eVolution rate of 91 $\mu$mol h$^{-1}$, whereas the commercial one exhibited a rate of 0.6 $\mu$mol h$^{-1}$, ca. 150 times lower than that for the $Nb_2O_5$ nanorod. Moreover, $Nb_2O_5$ nanorod superstructures maintained an almost constant photocatalytic $H_2$ production rate after 24 h. The higher performances were explained by the authors based on the superstructures of the material (Figure 2), in which photogenerated electrons could be transferred along the 1D nanorods direction and also transported to the neighboring nanorods, leading to a more efficient separation of photogenerated charge carriers.
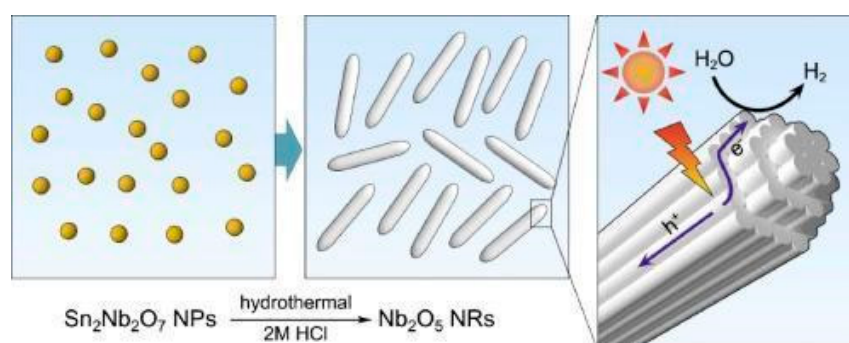


**Figure 2.** Scheme of $Nb_2O_5$ nanorod superstructures synthesis and the improved photogenerated charge carries separation. Reproduced with permission from the authors of [24]. Copyright (2019), Elsevier, Amsterdam, Netherlands.

Clearly, such morphological and structural transformations lead to changes in the optical and electronic properties of niobium oxide. In this sense, Zhang et al. reported an enclosed porous structure of pseudo-hexagonal tief-tief (TT) $Nb_2O_5$ nanowires, which showed a significant decrease in the band gap from 3.22 to 2.95 eV in relation to the nonporous $Nb_2O_5$ nanowires, and then an enhancement of $H_2$ eVolution under visible light irradiation ($\lambda$ > 420 nm) [25]. The material was prepared by a solvothermal synthesis using ammonium niobate(V) oxalate hydrate and oleic acid mixed with trioctylamine. The sample was calcined at different temperatures. Thermal treatment at 600 °C and 700 °C causes the formation of orthorhombic phase, while at 580 °C, the pristine TT-phase was formed, so this last condition was selected for further analysis. In TEM images, it was observed that the porous nanowires were shorter than 1 $\mu$m and exhibited well separated pores inside the structure, whereas nonporous ones were longer than 5 $\mu$m and showed ripple-like contrast owing to bending-induced strain. The authors could explain the formation of such porosity to the replacement of oxalate anion by oleic acid and trioctylamine in the Nb center, resulting in a structure with hydrophobic core and surrounding Nb species. Then, the subsequent heating treatment induced the formation of pores from the cores and the $Nb_2O_5$ crystalline nanowires from the coordination structure. However, the samples were not characterized by isotherms of $N_2$ adsorption to be properly classified as porous material. The authors suggested that under-coordinated ions in the twisted lattice around the pores could generate mid-gap states, and hence lower band gap energies. As a result, the $H_2$ production rate of the porous sample was 243.8 $\mu$mol g$^{-1}$ h$^{-1}$, considerable higher than the nonporous one, which exhibited $H_2$ eVolution rate of 113.1 $\mu$mol g$^{-1}$ h$^{-1}$ under similar conditions, and eVen higher than that for P25 $TiO_2$ (129.6 $\mu$mol g$^{-1}$ h$^{-1}$).

Besides the morphology, other strategies can be applied to increase the photocatalytic activity of $Nb_2O_5$ species. The introduction of defects into the crystal lattice could be used to engineer the electronic transport properties along the oxide structure or eVen to create new trap states inside the forbidden band gap region [26]. Zhao and coauthors reported improved solar-light absorption

via partial reduction of $Nb_2O_5$ nanorods with active exposed (001) surfaces, which result in the black niobium oxide [27]. In summary, the previous prepared $Nb_2O_5$ was thermally treated in an aluminum reduction device, where the sample and aluminum powder were positioned independently in a two-zone tube oven, and then the $Nb_2O_5$ and aluminum powders were heated to 500 °C and 800 °C, respectively. This procedure led to the formation of $Nb^{4+}$ centers and hence substantial oxygen vacancies that resulted in a black powder, and thus an enhancement in visible and infrared light absorption compared with the pristine $Nb_2O_5$. The reduction of $Nb_2O_5$ could be confirmed by Raman and X-ray photoelectron spectroscopies. The $Nb^{4+}$ centers were also characterized by electron paramagnetic resonance. High resolution transmission electron microscopy indicated predominant (001) crystal plane exposed on the nanorod surfaces, suggesting good crystallinity of samples before and after reduction. The samples were eValuated as photoanode using dip-coated FTO glasses in a 1 M NaOH electrolyte under 100 mW cm$^{-2}$ illumination with a 150 W Xe lamp. At 1.23 V, the reduced $Nb_2O_5$ sample showed a photocurrent density 138 times higher than that for $Nb_2O_5$. The carrier density was calculated by Mott–Schottky plots and was $3 \times 10^4$ times higher for the reduced sample, eVidencing an enhanced electrical conductivity, charge transport, and separation. Finally, the samples were eValuated to produce $H_2$ with 0.5 wt% Pt and 20% methanol solution under full-sunlight irradiation from a 300 W Xe lamp, which, for the reduced $Nb_2O_5$, resulted in 13 times higher production rate of 274.8 μmol h$^{-1}$ g$^{-1}$ in comparison with $Nb_2O_5$ nanorods (21.1 μmol h$^{-1}$ g$^{-1}$).

An extended visible light activity of orthorhombic $Nb_2O_5$ was achieved by Kulkarni et al. as result of nitrogen doping using a solid state reaction of urea and niobium salt [20]. At 500 °C, ammonia is released and works as nitrogen source to be introduced into the $Nb_2O_5$ lattice, filling oxygen vacancies. Field emission scanning electron microscopy (FE-SEM) analysis showed that the urea concentration was crucial for the observed morphologic changes. Concerning the optical properties, the modified samples were analyzed by UV/vis diffuse reflectance and compared to the pristine $Nb_2O_5$, which had a band gap energy of 3.4 eV. In general, all the N-doped $Nb_2O_5$ samples showed significant absorption in the range of 400–600 nm and a higher red shift in the band gap absorption when the urea concentration was increased (2.6–2.4 eV). Density functional theory (DFT) calculations described that N 2p bands falls above the O 2p bands, and so the top of the valence band gives rise to the reduction in the band gap. At the highest Nb/urea ratio investigated (1:15), this trend was not observed and a higher band gap edge than the expected trend (2.5 eV) was obtained. This would have resulted from nitrogen saturation of the niobia matrix. Photoluminescence measurements indicate that the optimal Nb/urea ratio was 1:10. This sample exhibited the lowest luminescence intensity among the other samples, indicating the efficient electron/hole separation. These results were in agreement with the photocatalytic $H_2$ eVolution experiments.

Another strategy to achieve higher photocatalytic performances is coupling to different $Nb_2O_5$ compounds with special attributes to create an efficient heterostructured photocatalyst. Owing to its flexibility in morphological, electronic, and structural properties, $Nb_2O_5$ is a promising candidate to design an effective heterojunction. Huang and coauthors reported a synergic combination of highly ordered mesoporous $Nb_2O_5$ (MNb) nanostructure to two-dimensional N-doped graphene (NGR) through a good interfacial connection (Figure 3) [28]. UV/visible diffuse reflectance spectroscopy eVidenced gradual shifts to longer wavelengths as the NGR quantity was increased, so the band gap energies were shift from 3.12 eV up to 2.67 eV. Photoluminescence analysis suggested that NGR supported an efficient separation of charge carriers owing to the fast electron transfer from the conduction band (CB) of MNb to NGR sheets.

Huang and coauthors reported an in situ growth of mesoporous $Nb_2O_5$ microspheres on the surface of g-$C_3N_4$ [21]. In this case, assuming the photocatalytic activity of g-$C_3N_4$ under visible light, the enhanced photoactivity was mainly achieved thanks to the effective interfacial charge transfer between g-$C_3N_4$ and $Nb_2O_5$. Therefore, it is mandatory to ensure sufficient interfacial contact, and this condition was succeeded by the authors via a so-called in situ self-assembly process of synthesis. The introduction of $Nb_2O_5$ microspheres on g-$C_3N_4$ caused an expressive enhancement

on the specific surface area. UV/visible diffuse reflectance spectroscopy showed that g-$C_3N_4$ and the composites presented an absorption edge at ca. 450 nm, while pure $Nb_2O_5$ had slight a band edge of ca. 420 nm. The slightly visible light absorption of $Nb_2O_5$ was justified by traces of carbonate species from the thermal decomposition of the triblock copolymer used in the synthesis. Photoluminescence spectroscopy eVidenced that pure g-$C_3N_4$ exhibits stronger emission than the composites. Photocatalytic activities for $H_2$ eVolution over the samples were eValuated and the composite with 38.1 wt% of $Nb_2O_5$ exhibited the highest $H_2$ eVolution rate. With higher amounts of the $Nb_2O_5$ (69.6 wt%), the photocatalytic performance was still higher than pure g-$C_3N_4$, but slightly decreased in relation to the composite with 38.1 wt% of $Nb_2O_5$. This fact could be related to a less effective interfacial contact between the two semiconductors and to a considerable reduction of light absorption by the composite. Other successful combinations between $Nb_2O_5$ and g-$C_3N_4$ are reported elsewhere [29,30].
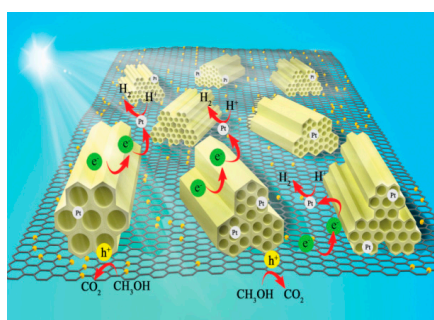


**Figure 3.** Schematic illustration of the transfer of photoexcited electrons and production of $H_2$ photocatalyzed by MNb–N-doped graphene (NGR) under visible light. Reproduced with permission from the authors of [28]. Copyright (2019), The Royal Society of Chemistry, London, United Kingdom.

Therefore, it can be observed that $Nb_2O_5$ pristine or modified has been employed successfully as a photocatalyst for $H_2$ eVolution. The role of the crystalline phase, morphology/shape, defects/oxygen vacancies, and heterojunction formation were investigated and showed great contributions for $H_2$ eVolution activity of $Nb_2O_5$.

## 2.2. Niobium Layered Compounds

Layered niobates are composed by a repetition of [$NbO_6$] octahedral units connected through adjacent or opposite sharing edges or corners, resulting in an extended 2D layered arrangement. This configuration is built by the stacking of negative charged layers separated by cations in the interlayer space [11,31]. The first niobate phases were reported in 1955 by Reisman and Frederic [32]. In this work, they could investigate the products $K_3NbO_4$, $KNbO_3$, $K_4Nb_6O_{17}$, $KNb_3O_8$, and "$K_6Nb_{44}O_{113}$" from the reaction of $K_2CO_3$ and $Nb_2O_5$ by differential thermal analysis [32,33]. Then, in 1969, the $K_4Nb_6O_{17}$ and $KNb_3O_8$ crystals were further investigated by Nassau and coauthors [33]. In 1982, a new series of phases $MCa_2Nb_3O_{10}$ (M = Li, Na, K, Rb, Cs, $NH_4$, Tl) was reported by Dion et al. [34]. Similarly, some years later, Jacobson and coauthors were able to prepare and investigate the interlayer reactivity of the series of layered compounds $K[Ca_2Na_{n-3}Nb_nO_{3n+1}]$ [35]. Since then, a class of layered perovskite with the general formula $A_x[B_{m-1}Nb_nO_{3n+1}]$ is known as Dion–Jacobson compounds (where A represents an alkaline monocation; B an alkaline earth ion; $m$ = 1, 2, and $2 \leq n \leq 7$; $n$ indicates the number of [$NbO_6$] chains that form each perovskite-like slab) [11]. Moreover, plenty of different niobates are currently known such as alkali ($M^+NbO_3$), columbite ($M^{2+}Nb_2O_6$), and rare-earths orthoniobates ($YNbO_4$) [6].

These materials are known as promising photocatalysts not just because of their different structures and band gap energies, but also their extended 2D layered arrangement, which provides a considerable surface area and allows easy modification either by intercalation, superficial modification, or formation

of nanosheets and nanoscrolls through exfoliation with bulky *n*-alkylammonium salts mboxciteB11-catalysts-682272,B31-catalysts-682272,B36-catalysts-682272. Recently, our group investigated the influence of the medium, co-catalyst precursor, and heat treatment in the photoactivity of Pt-modified hexaniobate ($K_{4-x}H_xNb_6O_{17}$) for $H_2$ eVolution [31]. The effect of the Pt(0) precursor and the deposition method (absorption or impregnation) was also investigated. These different conditions of the samples' preparation mainly affected their configuration and morphology. At the end, the $H_2$ eVolution performance was dependent on those conditions, where a 'soft' photoreduction of platinum precursors was identified as the best method for the preparation of those photocatalysts.

Suspended hexaniobate layers ($K_{4-x}H_xNb_6O_{17}$) in tetrabutylammonium hydroxide (TBAOH) showed a good performance in designing the photocatalytic film through the layer-by-layer (LbL) deposition technique [36]. Thin films were assembled by alternative immersions of FTO substrate into exfoliated hexaniobate with pre-adsorbed $[Pt(NH_3)_4]^{2+}$ suspension (pH = 8) and poly(allylamine hydrochloride) solution (pH = 4) up to 25 bilayers. Further thermal treatment at 500 °C removed the organic species, leading to a fuzzy assembly of hexaniobate nanoscrolls with Pt eVenly distributed in the surface, as shown in the FE-SEM image (Figure 4). In this case, it could be concluded that the scrolled morphology was favored in relation to the opened sheets. The Nb-based films were photoactive to produce $H_2$ from 20% (*v/v*) methanol/water solutions under UV-irradiation. The bare hexaniobate LbL films were able to photocatalyze the $H_2$ eVolution, with the apparent quantum yield being proportional to the number of deposited bilayers. This behavior eVidence that no photocatalytic surface is lost owing to material deposition. Moreover, when the Pt nanoclusters were added to the film composition, the observed $H_2$ eVolution rates were approximately two times higher, reaching 4.0% ± 0.5%.
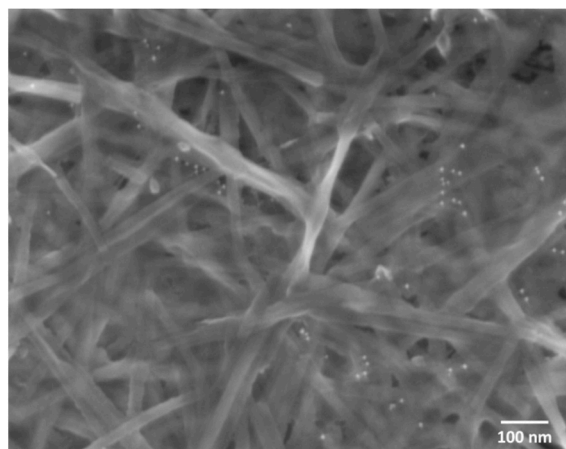


**Figure 4.** FE-SEM image of the surface of Pt-modified hexaniobate layer-by-layer (LbL) films with 25 bilayers (the bright small spots are Pt nanoclusters). Reproduced with permission from the authors of [36]. Copyright (2019), Elsevier, Amsterdam, Netherlands.

Oshima and coauthors reported the photocatalytic activity of Pt-deposited $KCa_2Nb_3O_{10}$ for water splitting [37]. With an adsorption method, cationic precursor of Pt ($[Pt(NH_3)_4]Cl_2$) was attached on niobate surface (1.3 wt%) by the $TBA^+/Ca_2Nb_3O_{10}^-$ suspension, followed by restacking with potassium hydroxide and reduction with $H_2$ gas in various temperatures. The authors noted that the deposition of Pt occurred in the interlayer spaces of the restacked nanosheets. Additionally, the increase in the annealing temperature up to 973 K decreased the Pt content in the $KCa_2Nb_3O_{10}$ interlayer space. Diffuse reflectance and X-ray photoelectron spectroscopies suggested that the adsorbed Pt was reduced from an oxidized to the metallic state according to the applied temperature, and that interlayer Pt species were less susceptible to reduction. The samples were eValuated for water splitting in NaI 10 mmol $L^{-1}$ solution and using a 300 W xenon lamp ($\lambda \geq 300$ nm). The maximum rate of both $H_2$ and $O_2$ production was achieved with the sample treated at 473 K, and higher reduction temperatures

led to a decline in the photoactivity. This fact could be explained by an improved contact between Pt and the niobate and the formation of suitable active sites. At higher temperatures, the Pt species were located mostly at the external surface. The authors also investigated the impact of the Pt valence state on water splitting activity, comparing the performance of samples heated at the 573 K under $H_2$ and air atmosphere. By TEM, both methodologies led to the formation of Pt with the same size. However, more electron-deficient Pt species were identified on the sample treated in air, which performed a better overall water splitting reaction than the sample treated at $H_2$.

Distinct species to form the layered Dion–Jacobson materials $AB_2Nb_3O_{10}$ also play an essential role in the physical properties of the material and especially in their photocatalytic performance. From this point of view, Kulischow et al. investigated a family of layered Dion–Jacobson perovskite-type materials $AB_2Nb_3O_{10}$ (A = K, Rb, Cs and B = Ca, Sr, Ba) and their photocatalytic activity for hydrogen production [38]. Seven different niobate were prepared by the molten salt method mixing $BCO_3$ or $B(NO_3)_2$, (B = Ca, Sr, Ba), $Nb_2O_5$, $A_2CO_3$ with ACl (A = K, Rb, Cs), and at specific reaction temperatures (750–1200 °C). UV/vis diffuse reflectance revealed that the band gap energies varied only with different B-cations, seeming to be independent of A-cations. In the case of $Ca^{2+}$ as B-cation, the band gap value was 3.6 eV, whereas it was 3.3 eV for $Sr^{2+}$ and 3.0 eV for $Ba^{2+}$. This trend suggested a dependence on the ionic radii of the B-cations that filled the spaces among $NbO_6$ octahedral units. With bigger B-cation, the overlap of the Nb 4d orbitals was greater, stabilizing the conduction band energy and, as a result, the band was shifted negatively. The prepared niobates were eValuated for $H_2$ eVolution in 10% methanol aqueous solution without a co-catalyst, and then Rh was in situ photodeposited (0.05 wt% Rh loading) on the catalyst. Without co-catalyst, the $KCa_2Nb_3O_{10}$ sample exhibited the highest $H_2$ eVolution rate; however, after the Rh addition, the highest overall hydrogen production was achieved by $CsCa_2Nb_3O_{10}$. In this case, photocatalytic behavior was influenced by the type of the A-cation at the interlayer, suggesting a dependence on the ionic radii in the order Cs > Rb > K, with the exception of $RbSr_2Nb_3O_{10}$. The B-cation influenced the hydrogen generation rates owing to more cathodic conduction band edges in the order Ca > Sr > Ba.

Zhou and coauthors showed that the performance of $KCa_2Nb_3O_{10}$ for $H_2$ eVolution could be enhanced through a nitrogen and tetravalent niobium doping to generate yellow and black $[Ca_2Nb_3O_{10}]^-$ nanosheets [39]. After the preparation of $KCa_2Nb_3O_{10}$ by solid state reaction, the material was treated at 800 °C for 5 h under $NH_3$ flow, resulting in the black niobate ($N^-/Nb^{4+}$-codoped). The previous addition of a certain stoichiometric excess of $K_2CO_3$ prevented the formation of oxygen defect, and thus the reduction of $Nb^{5+}$ ions, which resulted in the yellow niobate (N-doped). Then, the samples were acid-exchanged, followed by the exfoliation reaction with tetrabutylammonium hydroxide (TBAOH). X-ray absorption fine structure (XAFS) data on the Nb K-edge (18.986 keV) of all the samples indicate that doping did not change the perovskite-type crystal structure, as all three samples showed very similar overall profiles. However, an increase of the pre-edge peak (18.985 keV) of black niobate could be attributed to the partial reduction from $Nb^{5+}$ to $Nb^{4+}$ and the increased Nb–N bonding for yellow niobate, whereas the black one, showing a simultaneous decrease of both Nb–O and Nb–N, could point out the dominating generation of oxygen vacancies during the ammoniation process without $K_2CO_3$ additive. The samples were eValuated for photocatalytic $H_2$ production using 20 vol% methanol aqueous solution under full range irradiation with an Xe lamp. Undoped nanosheets show very low photocatalytic activity (11.4 mmol $h^{-1}$) compared with the activity of yellow and black niobate nanosheets (42.9 and 154.7 mmol $h^{-1}$, respectively). In this sense, the self-doping with $Nb^{4+}$ could significantly promote an enhanced separation efficiency of photogenerated carriers as well as the light absorption beyond single $N^{3-}$ doping. When Pt was loaded at 0.5 wt%, the $H_2$ eVolution rates were three times higher, 190.1 and 429.5 mmol $h^{-1}$ for yellow and black niobate nanosheets, respectively. The last one could achieve energy conversion efficiency for solar hydrogen production of 2.7%.

Later, the same group could also investigate the combination of elemental doping, liquid exfoliation, and composition control for a series of typical Dion–Jacobson phases $KCa_2Na_{n-3}Nb_nO_{3n+1}$

photocatalysts [40]. As seen in the scheme presented in Figure 5, $KCa_2Na_{n-3}Nb_nO_{3n+1}$ were prepared with various values of *n* in order to tune the thickness of the perovskite layer. Theoretically, using *n* = 3–6, the desired thickness of the layer should increase from 2.4 to 4.0 nm. The materials were obtained from the molar ratio of K/Na/Ca/Nb = 1.05/2/1.05(*n*−3)/*n* through calcination at 1200 °C, followed by the $N/Nb^{4+}$-doping via heat treatment under $NH_3$ flow. This method resulted in samples with different colors, varying from white to black. Samples before and after $NH_3$ treatment were analyzed by UV/vis diffuse reflectance, where red-shifts of the absorption edge were observed in all $N/Nb^{4+}$ doped samples. eVen after liquid exfoliation of bulk doped samples to obtain nanosheets, their suspension in water kept the colors from the bulk materials. TEM and atomic force microscopy (AFM) images revealed ultrathin sheets with several micrometers in size and thicknesses of 2.4, 2.8, 3.3, and 4.0 nm for the *n* = 3, 4, 5, and 6 homologues, respectively. The photocatalytic performance of the doped nanosheets was eValuated towards hydrogen eVolution from 20 vol% methanol solution under full arc irradiation (Xe lamp, 300 W). Considering all samples with and without 0.5 wt% Pt, the *n* = 4 product exhibited the highest $H_2$ production rate. This fact can be related to the migration length, which affects the electron–hole separation step. The higher photocurrent measurement was also found for *n* = 4 with a sequence of *n* = 4 > 5 > 3 > 6, which is consistent of $H_2$ eVolution experiments.
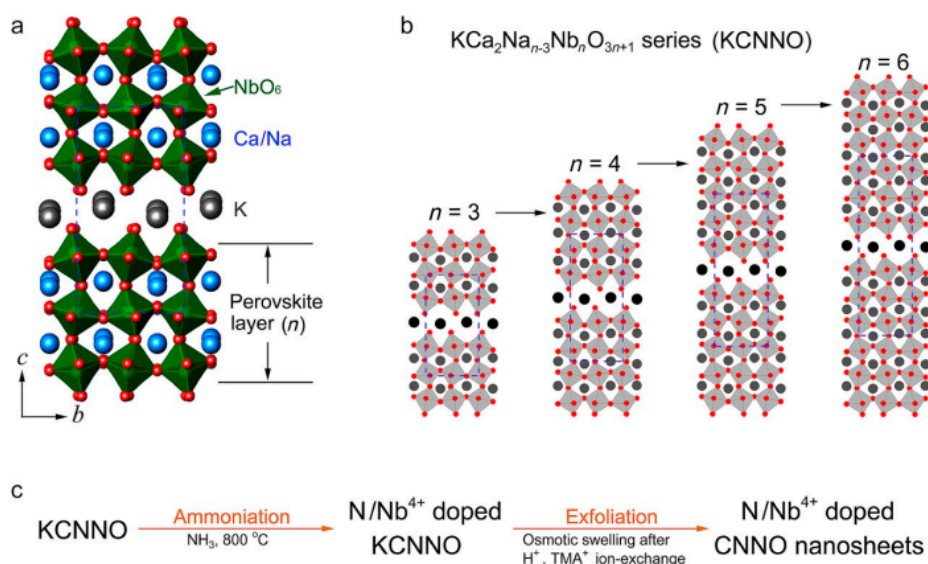


**Figure 5.** Schematic representation of (**a**) the general structure of $KCa_2Nb_3O_{10}$ (KCNNO), (**b**) $KCa_2Na_{n-3}Nb_nO_{3n+1}$ with thickness control of the perovskite layer by varying the *n* value, and (**c**) preparation of $N/Nb^{4+}$ codoped nanosheets (CNNO). Reproduced with permission from the authors of [40]. Copyright (2019), John Wiley & Sons, Inc., Hoboken, NJ, USA.

The photocatalytic activity of $HCa_2Nb_3O_{10}$ for hydrogen production was also extended for visible irradiation region by combination with CdS [41]. In this composite, after light excitation of CdS, the photo-generated electrons were transferred to the calcium niobate nanosheets thanks to their matched conduction band position of −1.32 eV for CdS and −1.18 eV for niobate (V vs. Ag/AgCl, pH = 7.0). So, the observed increase of the electron paramagnetic resonance (EPR) signal after illumination is the result of the efficient electron transfer that further induced the growth of oxygen vacancies. The samples were eValuated for photocatalytic $H_2$ eVolution in (0.1 M) $SO_3^{2-}$/(0.15 M) $S^{2-}$ solution under visible light, in which the exfoliated niobate was not able to be excited. The best performance was achieved by samples containing 53.6 wt% of CdS with a $H_2$ production rate of 16.5 μmol h$^{-1}$, about four times higher than pure CdS. Further increase of CdS resulted in lower activity, which was related to the aggregation of CdS nanoparticles. Later, a similar approach was applied by Hu and coauthors to design nanohybrid of CdS and $HCa_2Nb_3O_{10}$ and get photocatalytic $H_2$ production under visible light [42].

It has been shown that CdS has more negative conduction band energy than the employed niobate, indicating the spontaneous transfer of photoinduced electrons from CdS to niobate nanosheets.

Xiong and coauthors could improve the photocatalytic hydrogen production activity of $HNb_3O_8$ nanosheets by loading Cu with a facile photodeposition method [43]. Exfoliated $HNb_3O_8$ niobate was dispersed in $Cu^{2+}$ solutions with corresponding loadings of 2%, 1%, 0.5%, and 0.25% which was photodeposited in situ in triethanolamine solution. Firstly, the authors eValuated the samples for $H_2$ eVolution activity with 10 vol% of triethanolamine aqueous solution under the simulated solar light using a 300 W Xenon lamp. The photocatalytic performance increased after addition of $Cu^{2+}$ up to 0.5%, reaching the maximum rate of 59.1 $\mu$mol h$^{-1}$. With higher amounts of Cu, the shielding effect was detrimental for the photoactivity. In addition, when methanol was used as the sacrificial agent, the photocatalytic hydrogen production activity achieved the value of 98.2 $\mu$mol h$^{-1}$. The authors argued that in situ photodeposition induced selective deposition on the photocatalytic reduction sites of $HNb_3O_8$ nanosheets rather than arbitrary distribution.

The same type of niobate was recently applied to engineer a stable nanocomposite photocatalyst. Xia and coauthors reported a method to growth NiS in a highly dispersive way on the $HNb_3O_8$ surface [44]. In general, the random deposition and easy agglomeration in large particles of NiS are described as being problematic for the photocatalytic $H_2$ eVolution. Therefore, an electrostatic adsorption/self-assembly methodology was developed to obtain NiS on the $HNb_3O_8$ nanosheet as an efficient photocatalyst for the first time. The photocatalytic $H_2$ eVolution was performed with a 300 W Xenon lamp in a 10% triethanolamine (TEOA) aqueous solution, where the bare NiS and layered $KNb_3O_8$ showed no or very low $H_2$ production. In this condition, for the composite with 1 wt% NiS, the $H_2$ eVolution rate was 1519.4 $\mu$mol g$^{-1}$ h$^{-1}$, higher than the physical mixture of the components (582.5 $\mu$mol g$^{-1}$ h$^{-1}$). Time-resolved fluorescence decay analysis was applied to calculate the lifetime of the photogenerated electrons and holes. The kinetic data showed a slower decay for the composite, which indicates that the applied methodology resulted in more efficient utilization of photogenerated electrons and holes.

The potential of niobates structures for water splitting has also been demonstrated by some theoretical works. The perovskite-type niobate $NaNbO_3$ was selected by Wang and coauthors to investigate the effect of anionic monodoping with N, C, P, and S dopants, as well as with (N + N), (C + S), and (N + P) codoping pairs by hybrid density functional theory calculations [45]. At first, the direct band gap of pure cubic $NaNbO_3$ was predicted to be 3.30 eV, with the conduction band mainly formed by Nb-4d orbitals and valence band by the O-2p orbitals, and almost no Na-related states around the band edge were found, indicating that the Na atoms have negligible effects on the electronic structures near the Fermi level. In this sense, one of the O atoms in the cell was firstly substituted by one of four different species (N, C, P, and S), corresponding to a doping concentration of 2.5%. In the case of N-doped $NaNbO_3$, a hole would be generated as the N dopant has less valence electrons than the O atom. The higher energy of N-2p states (around 2.0 eV) induced a localized unoccupied impurity state above the Fermi level as well as several occupied impurity states around the valence band of $NaNbO_3$. For C doping, the substitution would result in two holes in the system, however, no unoccupied localized impurity states were found above the Fermi level. As a result, the total magnetic moment was higher and there were several impurity states above the valence band, which shifted up by about 1.58 eV. The doping with P resulted in a spin-polarized ground state as well, and, owing to the P-3p higher energy than the O-2p, several empty impurity states were found near the conductive band. When S was applied as a dopant, no empty states were found within the band gap, but several localized impurity states were localized below the Fermi level, right above the valence band of the niobate, which resulted in a narrowed band gap. This filled impurity states originated from the hybridization of S-3p and O-2p orbitals. Thus, the band gap values for N-, C-, P-, and S-doped $NaNbO_3$ were calculated to be 1.88, 1.61, 1.04, and 2.34 eV, respectively. Despite the narrower band gap energies, some disadvantages were observed as the undesirable empty gap states from N and P monodoping, which may act as trapping and recombination centers, and the elevated

valence band of $NaNbO_3$ after C doping, precluding the oxygen eVolution reaction. In this sense, the codoping possibility using pairs of (N + N), (C + S), and (N + P) was also investigated. It resulted in the band values as shown in Figure 6. In comparison with the pristine niobate, for (N + N) codoping, two fully filled states were generated within the band gap and its effective energy was 1.24 eV lower. The (C + S) dopping led to mid-gap states above the valence band of host system, and then a narrow band gap of 1.42 eV. For both systems, the band edges matched properly with the redox potentials of water, indicating that the photocatalyst would be suitable for overall photocatalytic water splitting. However, in the case of (C + S) codoping, the conductive band was shown to no be longer good for a spontaneous water splitting process eVen with a band gap value of about 1.33 eV. This study suggested that codoping can be a successful approach to improve the visible light photocatalytic performance of perovskite $NaNbO_3$.
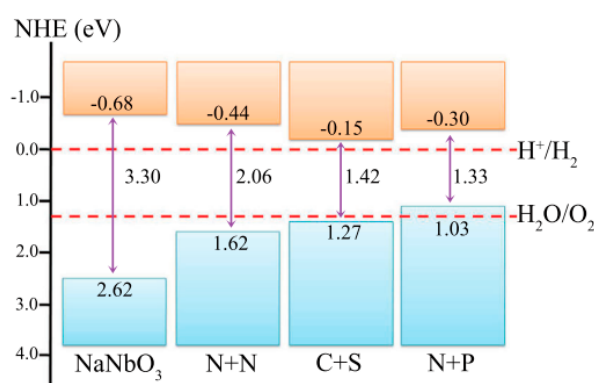


**Figure 6.** Band edge positions of the pure and codoped $NaNbO_3$. Reproduced with permission from the authors of [45]. Copyright (2019), John Wiley & Sons, Inc., Hoboken, NJ, USA. NHE, normal hydrogen electrode.

Kaneko and coauthors deeply investigated the origin of the visible light absorption and the optical band gap of 1.9 eV in the d1 metallic strontium niobate ($SrNbO_3$) [46]. By computational methods, firstly, they could verify at which electronic states the photoexcitation takes place, from CB → $B_1$ transition or $B_{-1}$ → CB ($B_{-1}$ denotes the band below the conductive band (CB), and $B_1$ denotes the band above the conductive band). By the band structures and projected density of states calculations, it was found that $B_{-1}$ state lies at around −4 eV and consists of O(p). Thus, from the atomic orbitals constituting each band, it was inferred that the optical gap corresponds to the Nb(d) → Sr(d)/Nb(d) transition, and so the optical gap was attributed to the CB → $B_1$ transition. The shifts of Fermi level as well as the changes in the optical gap concerning the Sr defects and O vacancies were investigated. The authors could conclude that the optical gap hardly depends on the amount of Sr defects. Sr and O are divalent cation and divalent anion, respectively, and the valence of the Nb ion constituting CB did not change eVen if the Sr defect and the O vacancy were produced in the same amount. Thus, if the valence of the Nb ions constituting CB does not change, the Fermi level will not shift either. Consequently, the optical gap, which is mainly caused by the excitation from the Fermi level to $B_1$, does not change by $Sr_{1-x}NbO_{3-x}$. In addition, in the case of $Sr_{0.875}NbO_3$ and $Sr_{0.875}NbO_{2.875}$, it was found that the latter eVidenced the dependence of the optical gap on the amount of Sr defects and its light absorption intensity was larger than that of the former.

Such doped niobates have been prepared and eValuated as photocatalysts. Yu et al. reported at first time the performance of carbon-doped $KNbO_3$ as well as the effect of $MoS_2$ addition in the material for photocatalytic $H_2$ eVolution [47]. Both pristine and C-doped $KNbO_3$ presented the orthorhombic phase, however, the latter resulted in peaks of 30–32° shifted to a lower angle, indicating that the carbon atom was doped into the lattice of $KNbO_3$. In addition, the C species were identified as $C^{4+}$ by X ray photoelectron spectroscopy (XPS) analysis, which meant that it did not replace the position of lattice oxygen. In addition, it was also confirmed that the substitution of $Nb^{5+}$ by $C^{4+}$ occurred and

also generated some oxygen vacancies to compensate the charge balance. The pristine niobate showed only UV light absorption with band gap of 3.07 eV. C-doped niobate presented very similar behavior, however, it showed a difference in the peak tailing in the range of 400–600 nm. The samples after the addition of $MoS_2$ in 0.2 wt% also presented the peak tailing in the visible-light region. $H_2$ eVolution was performed in methanol solution (20% *v/v*) under 300 W Xe lamp irradiation and in situ photodeposition of metallic Pt (0.37 wt%). The C doping of $KNbO_3$ could enhance the $H_2$ eVolution from 5 µmol $g^{-1}$ $h^{-1}$ to 142 µmol $g^{-1}$ $h^{-1}$ in comparison with the pristine sample. The decoration of $MoS_2$ on $C-KNbO_3$ could further increase the rate of $H_2$ eVolution to 1300 µmol $g^{-1}$ $h^{-1}$. The samples were also eVoluted under visible light, where pure niobate did not show activity, while $C-KNbO_3$ and $MoS_2/C-KNbO_3$ resulted in rates of 4.2 µmol $g^{-1}$ $h^{-1}$ and 9.3 µmol $g^{-1}$ $h^{-1}$, respectively. These activities were much lower compared with values under UV/vis light, indicating that the composite is more suitable for working in the UV region of irradiation.

Columbites are also founded in the literature with further applications in photocatalytic research. The effect of structural distortion of $SnNb_xO_y$ in comparison with the crystalline $SnNb_2O_6$ regarding the photocatalytic activity was investigated by Huang et al. [48]. The crystalline sample exhibits a band gap energy of 2.10 eV, while the band gap energies for disordered and amorphous samples were 2.33 eV and 2.43 eV, respectively. Furthermore, the electronic band gap could be tuned by the structural disorder engineering, as an increase of structural lattice disorder led to an increase of band gap energies. By XPS and UV/vis absorption analysis, the valence band edge of crystalline $SnNb2O6$ was about 1.42 V with the conduction band of −0.68 V, whereas for the disordered sample, the values were 1.98 V and −0.35 V, respectively. As a consequence, the latter exhibited $H_2$ eVolution rates 11 times and 1.7 times higher than that of crystalline and amorphous samples, respectively, under visible light irradiation ($\lambda \geq 420$ nm). The photoinduced charge carrier behaviors under pulse laser at 532 nm were investigated by transient absorption spectroscopy (TAS). The three samples presented broad and continuous absorption in the visible range at a delay time of 100 ns, indicating the separation of charge carries at different trap states. This behavior was especially pronounced in disordered $SbNb_xO_y$, which indicated a better charge separation. The transient absorption decay kinetics also expressed the same, with effective lifetimes for the amorphous, disordered, and crystalline samples of 0.52 ms, 0.56 ms, and 0.26 ms, respectively.

The influence of type of polymorph on the photocatalytic activity of $CuNb_2O_6$ columbite was further explored by Kamimura et al. [49]. Two different polymorphs, monoclinic and orthorhombic, revealed that the local crystal structure of the $CuO_6$ octahedral was strongly correlated to the optical absorption property. Both samples exhibited the same band gap, 2.7 eV. However, two additional broad bands in the near-infrared (NIR) region were observed for the orthorhombic sample, being ascribed to $Cu^{2+}$ d–d transitions in a distorted octahedral ligand field. In principle, this transition is forbidden by the Laporte selection rule owing to the symmetric $CuO_6$, but in the case of the orthorhombic phase, it was partially allowed because of the Jahn–Teller effects of orthorhombic $CuNb_2O_6$. The photocatalytic $H_2$ eVolution was performed using a 10 vol% methanol solution and an Air Mass (AM) 1.5G solar light irradiation. The two polymorphs of $CuNb_2O_6$ produced $H_2$ under these conditions, but the monoclinic sample was more active than the orthorhombic one. Thus, to elucidate if the d–d absorption affects the photocatalytic activity, the previous results were compared to those using a near-infrared (NIR) cutoff filter. When the monoclinic sample was tested, the rate of $H_2$ eVolution rate did not change expressively when the NIR filter was applied. In this case, the loss of 20% of activity could be explained by the low transmittance of the employed cutoff filter in the visible region. In contrast, the active for orthorhombic $CuNb_2O_6$ decreased 90% in relation to that observed without an NIR filter. On contrary to the monoclinic phase, which was insensitive to the excitation of the d–d transition in $Cu^{2+}$ ions, for the orthorhombic one, the electron $3d^9$ configuration of $Cu^{2+}$ readily induces structural distortion by Jahn–Teller effects in an octahedral crystal field. The empty 3d orbitals of $Cu^{2+}$ could work as deep traps for the photo-generated electrons, and thus increase the recombination rate, resulting in a significant decrease in photocatalytic activity in the presence of an NIR cut-off filter. With NIR photons,

the photo-generated electrons filled 3d orbitals of $Cu^{2+}$ via d–d absorption, a state that inhibited the recombination of photogenerated electrons in the conduction band. These distinct mechanisms were schematically represented on Figure 7. So, in the case of orthorhombic structure, the photocatalytic performance was dependent on fully filled Cu 3d-orbitals.
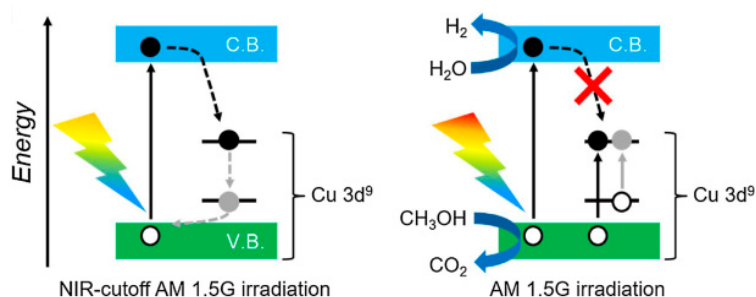


**Figure 7.** Photocatalytic process over orthorhombic $CuNb_2O_6$, comparing the presence and absence of near-infrared (NIR)-cutoff filter. C.B. and V.B. correspond to conduction band and valence band, respectively. AM 1.5G defines the employed irradiation conditions following the ASTM G-173-03 Standard. Reproduced with permission from the authors of [49]. Copyright (2019), Elsevier, Amsterdam, Netherlands.

Chun and coauthors employed a two-step hydrothermal process to form nanosized $ZnNb_2O_6$ columbite [50]. The samples were applied to photocatalytic $H_2$ eVolution in 20 vol% methanol under irradiation of 500 W high-pressure mercury lamp. The sample prepared by the new method produced an optimal activity of 23.6 $\mu mol\ H_2\ h^{-1}\ g^{-1}$, while a bulk $ZnNb_2O_6$ prepared by solid state exhibited a $H_2$ eVolution rate of 9 $\mu mol\ h^{-1}\ g^{-1}$. This fact was attributed to its appropriate crystallinity and high specific surface area (61 $m^2\ g^{-1}$). Further, the authors eValuated the effect co-catalyst deposition on nano-$ZnNb_2O_6$. In this case, both pristine water and methanol aqueous solution media were applied. In pure water, the bare photocatalyst showed an undetectable amount of $H_2$. The optimal co-catalyst was found to be Pt, as the $H_2$ generation rate achieved up to 680 and 3200 $\mu mol\ h^{-1}\ g^{-1}$ in pure water and methanol aqueous solution, respectively. Moreover, with the modified sample and at optimal conditions, a maximal apparent quantum yield (AQY) value of 4.54% was obtained in pure water. The value increases to 9.25% with the assistance of methanol as the sacrificial agent.

The manipulation of composition, morphological, and surface properties of three-dimensional hierarchical $Nb_3O_7(OH)$ superstructures was achieved through Ti(IV) incorporation, as reported by Betzler and coauthors [51]. Firstly, the undoped $Nb_3O_7(OH)$ consisted of blocks of corner-sharing $NbO_6$ octahedra, forming hollow cubic superstructures of nanowire networks (Figure 8a). When an average amount of 5.5% titanium was incorporated into the crystal lattice, it formed a spherical morphology, hollow and built up from nanowires as well (Figure 8b). With a higher amount of Ti(IV) (10.8%–31.2%), a cubic morphology with smaller nanowires arranged to form the walls of hollow cubes was observed (Figure 8c). All the samples presented the same nanowire arrangement; however, it became smaller, shorter, and flatter as the quantity of Ti was increased. Both XRD and energy-dispersive X ray (EDX) measurements indicated a homogeneous distribution of titanium, however, with more than 12% Ti, the crystal lattice of $Nb_3O_7(OH)$ was not able to accommodate it, and then the formation of niobium-doped anatase $TiO_2$ plates was favored for further titanium excess. The specific surface area was also affected and it changed from 79 $m^2\ g^{-1}$ for $Nb_3O_7(OH)$ (morphology a) to 132 $m^2\ g^{-1}$ and 173 $m^2\ g^{-1}$ for morphologies b and c, respectively. The three samples showed the same band gap energy of 3.2 eV, but an additional absorbance in the 550−850 nm region was observed, which came from oxygen vacancies in the $TiO_2$ plates. Further, the samples were eValuated to $H_2$ eVolution under an Xe lamp irradiation (600 $mW\ cm^{-2}$), with 10 vol% methanol and in situ photodeposited Pt at 8 wt%. The $Nb_3O_7(OH)$ resulted a rate of 870 $\mu mol\ g^{-1}\ h^{-1}$, and then, as the Ti concentration increases, the $H_2$ rates zre raised to 1773 $\mu mol\ g^{-1}\ h^{-1}$ for morphology b and 1988 $\mu mol\ g^{-1}\ h^{-1}$ for

morphology c. The same trend was also expressed by transient absorption measurements, where morphology a showed an averaged lifetime of 54 ± 2 ps, while morphologies B and C presented lifetimes of 64 ± 2 ps and 73 ± 4 ps, respectively. The authors explained this behavior by the fewer amounts of hydroxyl groups required for charge neutrality with the replacement of $Nb^{5+}$ by $Ti^{4+}$, as they are known for acting as non-radiative recombination sites. The doubled $H_2$ production rate of morphology b, compared with morphology a, was most likely the result of a combination of its fewer recombination sites and larger surface area. The further, but less pronounced increase of the $H_2$ production rate for morphology c came from the presence of $TiO_2$ plates, which did not have such a strong effect on the photocatalytic reaction.

It is clearly noted that niobates offer the possibility to be combined with innumerous co-catalysts. Previous cited works and other examples from the literature are summarized in Table 1.

**Table 1.** Summary of the photocatalytic activity of niobates combined with distinct materials towards $H_2$ eVolution from aqueous solution.

| Niobate | Co-Catalyst | Light Source | Sacrificial Reagent | $H_2$ Formation Rate | Ref. |
|---------|-------------|--------------|---------------------|---------------------|------|
| $HCa_2Nb_3O_{10}$ | CdS, Pt | 300 W Xe, >400 nm | Lactic acid | 52.6 $\mu mol\ h^{-1}$ | [41] |
| $HCa_2Nb_3O_{10}$ | CdS | 300 W Xe, >420 nm | methanol | 450 $\mu mol\ g^{-1}\ h^{-1}$ | [42] |
| $HNb_3O_8$ | $Cu^{2+}$ | 300 W Xe | methanol | 98.2 $\mu mol\ h^{-1}$ | [43] |
| $HNb_3O_8$ | NiS | 300 W Xe | triethanolamine | 1519.4 $\mu mol\ g^{-1}\ h^{-1}$ | [44] |
| C-doped $KNbO_3$ | $MoS_2$, Pt | 300 W Xe | methanol | 1300 $\mu mol\ g^{-1}\ h^{-1}$ | [47] |
| $H_{1.78}Sr_{0.78}Bi_{0.22}Nb_2O_7$ | $Ni-CH_3CH_2NH_2$ | 300 W Xe | methanol | 372.67 $\mu mol\ h^{-1}$ | [52] |
| $KNb_3O_8$ | $g-C_3N_4$ | 1000 W Hg λ > 400 nm | dimethylhydrazine | 25.0 $\mu mol\ h^{-1}\ g^{-1}$ | [53] |
| $K_3H_3Nb_{10.8}O_{30}$ | $g-C_3N_4$ | 1000 W Hg λ > 400 nm | dimethylhydrazine | 27.0 $\mu mol\ h^{-1}\ g^{-1}$ | [53] |
| $HNb_3O_8$ | $g-C_3N_4$ | 1000 W Hg λ > 400 nm | dimethylhydrazine | 37.0 $\mu mol\ h^{-1}\ g^{-1}$ | [53] |
| $Ca_2Nb_2TaO_{10}$ | $g-C_3N_4$, Pt | 300 W Xe, >400 nm | triethanolamine | 43.54 $\mu mol\ h^{-1}$ | [54] |
| $Ba_5Nb_4O_{15}$ | $g-C_3N_4$ | 3 W LEDs 420 nm | oxalic acid | 2673 $\mu mol\ h^{-1}\ g^{-1}$ | [55] |
| $AgNbO_3$ | $g-C_3N_4$, Pt | 300 W Xe, >420 nm | methanol | 88.0 $\mu mol\ g^{-1}\ h^{-1}$ | [56] |
| $KTa_{0.75}Nb_{0.25}O_3$ | $g-C_3N_4$, Pt | 300 W Xe, >420 nm | methanol | 86.2 $\mu mol·g^{-1}·h^{-1}$ | [57] |

Besides the previous cited materials, niobium is also flexible in terms of designing different layered compounds with distinct elements. Fujito and coauthors reported a visible light response of layered perovskite oxychloride $Bi_4NbO_8Cl$ for water splitting [58]. This material consists of single-layer $NbO_4$ perovskite units separated by $(Bi_2O_2)_2Cl$ blocks. It presented a band gap of 2.39 eV with valence and conductive bands of 2.11 eV and −0.28 eV, respectively. Experimental and theoretical results suggested that the valence band was formed by highly dispersive O-2p orbitals coming from the interactions within and between Bi−O and Nb−O slabs. As expected from the conductive band value, $Bi_4NbO_8Cl$ showed activity for $H_2$ eVolution from an aqueous methanol solution under UV irradiation (300 W Xe lamp) and Pt (0.5 wt%) loading. However, the obtained rate of ~0.1 $\mu mol\ h^{-1}$ was considered low and a higher performance for $O_2$ was found. Apparent quantum efficiency for $O_2$ eVolution was determined as ~0.4% with $FeCl_3$ as an electron acceptor, under monochromatic light at 420 nm (~25 mW/cm²). So, through a Z-scheme mechanism, the system was coupled to a $H_2$-evolving photocatalyst of Rh-doped $SrTiO_3$ and $Fe^{3+}/Fe^{2+}$. In this way, as in the schematic shown in Figure 9, a simultaneous eVolution of $H_2$ and $O_2$ under visible light was successfully observed.
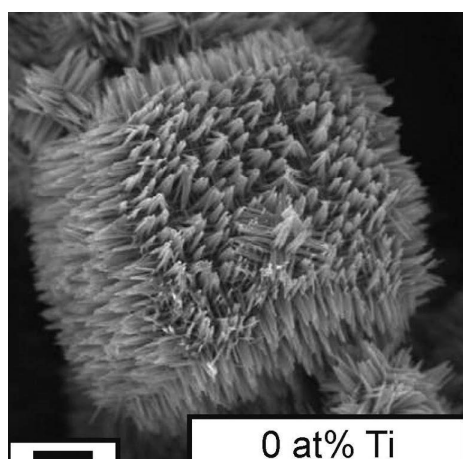
(**a**)
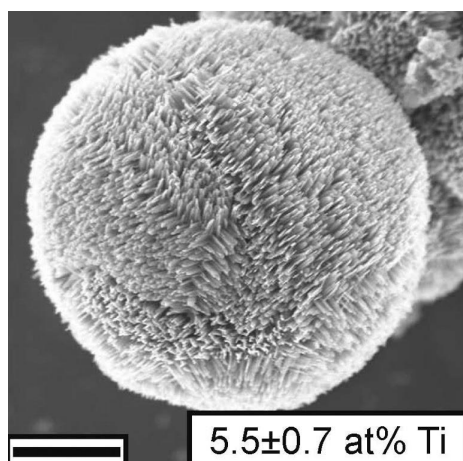


(**b**)
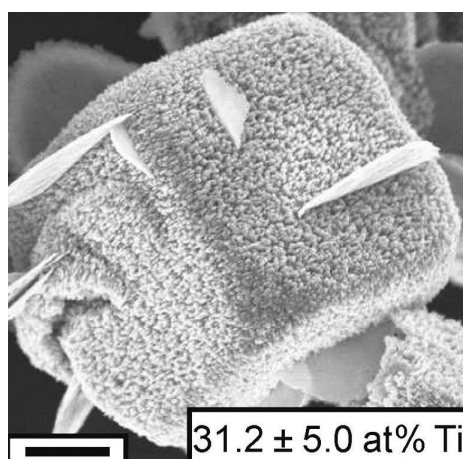


(**c**)

**Figure 8.** SEM images of (**a**) $Nb_3O_7(OH)$ and (**b**,**c**) Ti(IV) modified samples with the titanium content averaged over the morphology indicated relative to niobium (scale bar of 1 μm). Reprinted with permission from the authors of [51]. Copyright (2019) American Chemical Society, Washington, DC, USA.
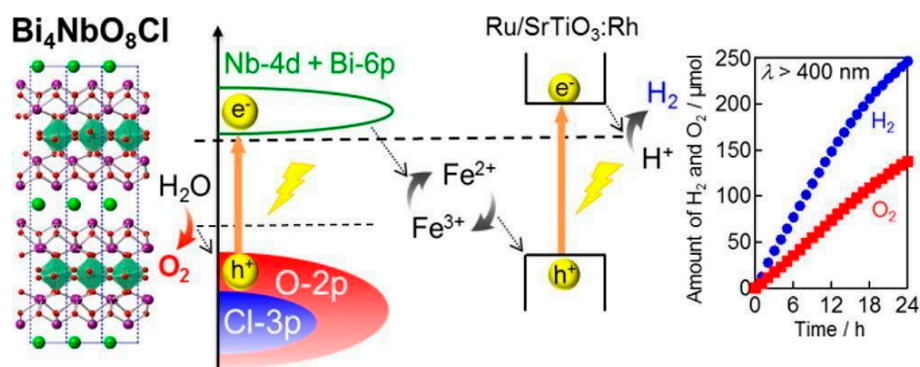
**Figure 9.** Scheme of Z-scheme water splitting of $Bi_4NbO_8Cl$ coupled with $Ru/SrTiO_3/Rh$ photocatalyst via $Fe^{3+}/Fe^{2+}$ redox mediator. Reprinted with permission from the authors of [58]. Copyright (2019) American Chemical Society, Washington, DC, USA.

Wakayama and coauthors reported a novel compound obtained from a mixture of layered $RbNdNb_2O_7$ and $Rb_2CO_3$ [59]. The new layered niobium oxynitride, $Rb_2NdNb_2O_6N$, resulted in a structure as $Rb_2NdNb_2O_6N$ $H_2O$ composed by double-layer $[NdNb_2O_6N]^{2-}$ perovskite slabs separated by two Rb cations and one $H_2O$ molecule. The material showed a band gap of 2.5 eV with visible light absorption, whereas the precursor $RbNdNb_2O_7$ essentially absorbs UV light with a band gap energy of 3.7 eV. In the former case, additional N 2p orbitals in the valence-band formation caused a valence-band maximum that was much more negative. In contrast, as the conduction band consists mainly of Nb 4d orbitals, its value remained basically unaffected. Thus, the $H_2$ eVolution was eValuated in the presence of TEOA as an electron donor in dimethyl sulfoxide (DMSO) containing 1 mL of water. The sample was irradiated with visible light ($\lambda$ > 400 nm) by 300 W xenon lamp, and Pt was previously deposited at 0.5 wt%. As shown in Figure 10, a stable $H_2$ eVolution was observed for 20 h from the $Rb_2NdNb_2O_6N$ sample, in contrast to the precursor, which did not show a response under visible light irradiation.
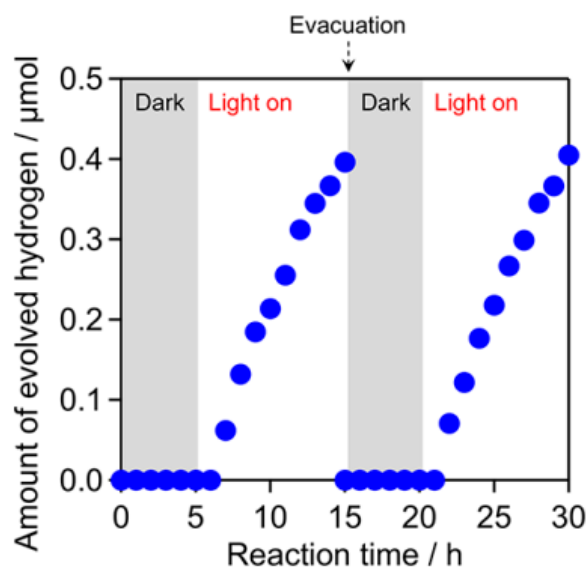


**Figure 10.** $H_2$ eVolution over $Pt/Rb_2NdNb_2O_6N$ in DMSO/TEOA solution containing 1 mL of water. Reprinted with permission from the authors of [59]. Copyright (2019) American Chemical Society, Washington, DC, USA.

Therefore, it can be observed that niobium layered compounds form a versatile Nb-based materials class that exhibits great activity for $H_2$ eVolution reaction. Additionally, several procedures to tuning

the photocatalytic performance niobium layered compounds were discussed, such as changes in the structural and morphology, doping and co-doping, and combination with other semiconductors.

## 2.3. Nb-Doped Materials

Two of the main drawbacks in the photocatalysis heterogeneous are the rapid recombination of electron/hole pair and semiconductor activation only under UV irradiation. A strategy to increase the photocatalytic performance of semiconductors by overcoming these challenges is the introduction of impurities able to change the electronic behavior of the material, in one word, the doping. Niobium is well known in the literature as a dopant agent, especially for titanium-based semiconductors, as its higher charged ion can substitute the $Ti^{4+}$ site in the oxide structure, and simultaneously play the role of donor, improving carrier concentration and conductivity [60]. For $TiO_2$, the defect state provided by the doping is located upon the conduction band minimum and contributes electrons to the unoccupied Ti 3d orbital without introducing additional states in the bandgap. However, in order to satisfy the charge compensation, the substitution can be accompanied by the incorporation of other defects as oxygen vacancies or eVen $Ti^{3+}$ defects below the conductive band, which lead to a visible range absorption [61]. In Table 2, examples of Nb-doped semiconductors for $H_2$ eVolution are listed.

**Table 2.** Summary of Nb-doped photocatalysts employed for $H_2$ eVolution from aqueous solution.

| Semiconductor | Co-Catalyst | Light Source | Sacrificial Reagent | $H_2$ Rate | Ref. |
|---|---|---|---|---|---|
| $TiO_2$ | - | 300 W Xe > 420 nm | ethanol | 1146 $\mu mol\ g^{-1}$ | [15] |
| $TiO_2$ | Pd | 500 W Hg-Xe 420–680 nm | methanol | ~0.6 mmol $g^{-1}\ h^{-1}$ | [62] |
| $TiO_2$ | Pt | 500 W Hg-Xe 420–680 nm | methanol | ~0.1 mmol $g^{-1}\ h^{-1}$ | [62] |
| $TiS_3$ | - | 200 W halogen | $Na_2SO_3$ (electrolyte) | 2.2 $\mu mol\ min^{-1} \cdot cm^2$ | [63] |
| $Cu_5Ta_{11}O_{30}$ | Pt | 1000 W Xe arc > 420 nm | methanol | 6 $\mu mol\ h^{-1}$ | [64] |
| $Ta_3N_5$ | - | 400–700 nm | water | 41.4 $\mu mol\ g^{-1}\ h^{-1}$ | [65] |
| $KTaO_3$ | Pt | 300 W Xe | methanol | 728 $\mu mol\ g^{-1}\ h^{-1}$ | [66] |
| $BiVO_4$ | - | 100 mW $cm^{-2}$Xe | $NaHCO_3$ (electrolyte) | 0.18 mmol $h^{-1}$ | [67] |

The performance of the Nb-$TiO_2$ photocatalyst was eValuated using various sacrificial agents such as methanol, ethanol, and 2-propanol by Fontelles-Carceller [68]. The photocatalyst was prepared with an Nb/Ti ratio of 0.025:0.975, which was confirmed by XPS measurements. In principle, the presence of Nb does not significantly change the band gap (3.15 eV) or the specific surface area (80.5 $m^2\ g^{-1}$) of the photocatalyst in comparison with pure $TiO_2$ (3.18 eV of band gap and 82.1 $m^2\ g^{-1}$ of surface area). The $H_2$ eVolution was investigated by the photocatalysts loaded with 0.5 wt% of Pt in presence of a 3:7 (*v/v*) alcohol/water mixture under irradiation of an Hg-Xe lamp (500 W). For both $TiO_2$ and Nb–$TiO_2$, the maximum rates were observed for methanol, followed by ethanol and 2-propanol. In all tested conditions, as shown in Figure 11, the doped sample showed a significantly better result than the non-doped sample. Both samples presented maximum rates for methanol, followed by ethanol and 2-propanol. In addition, the products formed during the photocatalytic reaction were investigated and, for methanol and ethanol, basically the same compounds were identified. Both samples generated formic acid and metyl formate by methanol oxidation with the addition of formaldehyde for the Nb-doped sample under UV illumination. When ethanol was applied, in all conditions of irradiation and applied samples, acetaldehyde and ethyl acetate were found. Nevertheless, when 2-propanol was applied as a sacrificial reagent, the Nb-doped sample generated acetone and propanone–diisopropyl–acetal, whereas bare $TiO_2$ produced only acetone. So, it was possible to affirm that the presence of Niobium at the surface eVen in a small proportion was

able to generate a new compound not observed for the pristine sample. In this sense, in situ infrared studies were also carried out under dark and illumination conditions and in the presence of the alcohol in water vapor. In principle, under the dark, it was possible to verify the adsorption of the alcohols on the surface of both samples. Under UV irradiation, the infrared spectra showed that alcohol and alcoxy species were consumed and/or desorbed from the surface of the samples. For methanol and ethanol, carboxylate/carbonate species were found as the main surface product. This could indicate the attack from hole to the alcohol to form oxidized species related to the corresponding alcohol/alcoxy adsorbed species. In the case of 2-propanol, carboxylate species were less present at the surface owing to the low coverage of products from the relatively easy desorption of acetone. Regarding the $H_2$ eVolution, the authors suggested that the differences in activity are correlated quantitatively with the average oxidation potential of the alcohol. When comparing methanol with ethanol using infrared spectroscopy, they showed essentially the same behavior of the titania surfaces against the alcohol and eVolving molecules coming from the hole-attack.
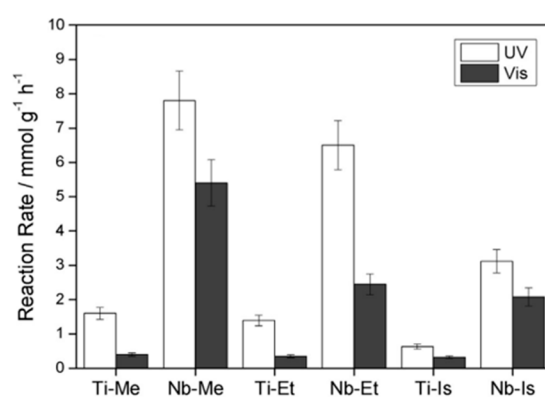


**Figure 11.** Reaction rate of the hydrogen photoproduction using different alcohols. Me, Et, and Is stand for methanol, ethanol, and 2-propanol (isopropanol), respectively. Reproduced with permission from the authors of [68]. Copyright (2019), Elsevier, Amsterdam, Netherlands.

Different materials that were doped by niobium ions to make them able to split water have been reported in the literature. The improvement of $WO_3$ for water splitting by photoelectrochemical process was achieved by Nb-doping [69]. The morphology of the material turned from nanorod to nanotriangle, which also increased the porosity of the $WO_3$ films. Also, the band gap increased to 2.74 eV by Nb-doping in comparison with $WO_3$ (2.63 eV) and additional oxygen vacancies were induced. Besides that, the carrier densities significantly increased from ~$3.44 \times 10^{19}$ cm$^{-3}$ to $1.27 \times 10^{22}$ cm$^{-3}$, indicating that $Nb^{5+}$ ions act as donor dopants in the $WO_3$ lattice. It could improve the charge separation and electron transport, and then the doped sample exhibited higher photocurrent, incident photon to charge carrier efficiency (IPCE) (39% to 52% at 300 nm and 1.23 V vs. RHE), and photoconversion efficiencies.

Also, with the objective to promote photoelectrochemical water splitting, niobium could support the activity of $BiVO_4$ films [67]. In this case, the authors concluded that $Nb^{5+}$ ions were not placed in the crystalline structure of $BiVO_4$, rather as niobium oxide or oxochloride. Firstly, the addition of 10% of Nb(V) resulted a higher IPCE, which reached 75% in comparison with pristine $BiVO_4$ of 55% at 2.08 V versus RHE (380–550 nm). The $H_2$ eVolution experiments were run by an H-shaped cell with pristine or modified $BiVO_4$ film as a photoanode coupled with a cathode of Pt and carbon paste. After 16 h of irradiation at 2.08 V, the pristine sample reached a maximum $H_2$ eVolution rate of 0.09 mmol h$^{-1}$, whereas Nb-modified $BiVO_4$ increased about two times to 0.18 mmol h$^{-1}$. The authors argued that the higher performance of the modified sample would be related to the modification of the nanostructure of the film, but also owing to other effects not obvious by the obtained data. A high efficiency for the photoelectrochemical water splitting reaction was achieved by doping of $SnO_2$ nanotubes (NTs) with Nb and N co-doping [70]. Niobium could be ascribe as an effective dopant

owing to its abundant electronic states and lower ionic radii of $Nb^{4+}$ (69 pm) compared with $Sn^{4+}$ (71 pm), resulting in minimum lattice strain. As shown in Figure 12a, the addition of Nb could improve the absorption of light at lower wavelengths, suggesting a decrease in the band gap of the doped samples, with an increase in Nb content. Then, a further doping with N could result in a significant decrease of band gap to 1.99 eV from 3.1 eV of $(Sn_{0.95}Nb_{0.05})O_2$. The lowering of the optical band gap for this sample could provide an IPCE of 10% at 500 nm and potential of ~0 V (vs. RHE), which was described by the author as the highest IPCE value obtained for semiconductor materials explored so far for photoelectrochemical (PEC) water splitting. The generated $H_2$ and $O_2$ gases at the cathode (Pt wire) and the photoanode are shown in Figure 12b. The theoretical concentration of $H_2$ from Faraday's Law was also calculated, which was very similar to the experimental one, suggesting a Faradaic efficiency close to 100%. Besides that, the ratio of produced gases was around 2, showing a stoichiometric decomposition of water into $H_2$ and $O_2$. From these as well as the theoretical results, it was possible to conclude that the Nb and N co-doping in $SnO_2$ afford better light absorption properties, increased carrier density, and facile electrochemical charge transfer.
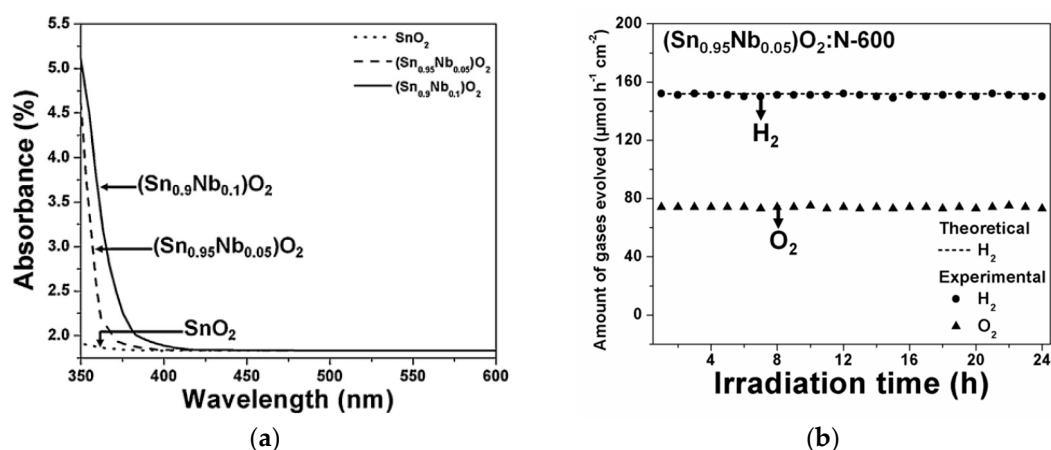


(a)                                              (b)

**Figure 12.** (**a**) UV/vis absorption spectra of $SnO_2$ NTs and $(Sn_{1-x}Nb_x)O_2$ NTs (x = 0.05, 0.1) and (**b**) theoretical $H_2$ gas and measured $H_2$ and $O_2$ gases, during 24 h chronoamperometry test of $(Sn_{0.95}Nb_{0.05})O_2$/N performed in 0.5 M $H_2SO_4$ solution at 0.75 V (vs. RHE) and 26 °C. Reproduced with permission from the authors of [70]. Copyright (2019), Elsevier, Amsterdam, Netherlands.

## 3. Photoreduction of $CO_2$

*Artificial Photosynthesis*

Carbon dioxide ($CO_2$) emission from fossil fuels is the main concern when discussing global warming and related climate changes. Because the global energy demand will continue to increase, the consumption of fossil fuels will continue to be high for the next few decades, which undoubtedly brings the necessity of large-scale $CO_2$ mitigation from the atmosphere [71]. The observation of natural photosynthesis in green plants motivated the development of photocatalytic $CO_2$ reduction (artificial photosynthesis), which is one promising solution to transform the current fossil fuel-based economy into $CO_2$-neutral energy systems using the sustainable "photon" economy and mitigate the greenhouse gas effect [3,72–74]. Another advantage of the photocatalytic $CO_2$ reduction is the indirect solar energy storage on carbon-based molecules. Therefore, the artificial photosynthesis acts as killing two birds with one stone in view of protecting the environment and simultaneously supplying renewable energy. However, $CO_2$ is very stable/inert regarding chemical reactions, meaning that $CO_2$ conversion demands a considerable amount of energy; therefore, it is quite difficult to convert it to reusable chemicals [75].

In the beginning of the 1900s, Giacomo Ciamician published a seminal paper with the first idea about the artificial photosynthesis, with the suggestion that society should shift from consuming fossil fuels to generating sustainable energy from the sun [76]. Later, Inoue et al. reported the

photoelectrocatalytic reduction of $CO_2$ to form organic compounds such as formic acid, formaldehyde, methyl alcohol, and methane. In the presence of various semiconductors, the dependence between the formed products and the semiconductor conduction band energy was demonstrated [77].

The $CO_2$ photoreduction process is a multielectron process (2, 4, 6, or 8 electrons) that can yield diverse products and occurs through different steps that involve adsorption, activation, and dissociation of the C=O bond. The adsorption and activation step is especially challenging because $CO_2$ is highly stable and inert [78]. In Table 3, some of the possible $CO_2$ reduction reactions are summarized along with their respective redox potentials. Selected potentials are compared with Nb-based photocatalysts at Figure 13. The formation of first intermediate ($CO_2^{\bullet-}$) state imposes a significant energy to the reaction and is frequently identified as the rate determining step. Once $CO_2^{\bullet-}$ is formed, it may be subsequently reduced via the protonation of its oxygen atom, resulting in the formation of $^{\bullet}COOH$. This intermediate can be reduced to CO and released from the semiconductor surface. Alternatively, $CO_2^{\bullet-}$ may also be reduced via the protonation of its carbon atom to form $HCOO^{\bullet}$, which is further reduced to formate ($HCOO^-$) [79–81]. Therefore, the $CO_2$ reduction mechanism is very complex and imposes kinetic and thermodynamic limitations.

**Table 3.** Common products from $CO_2$ reduction, their simplified half reactions, and redox potentials at pH = 7.

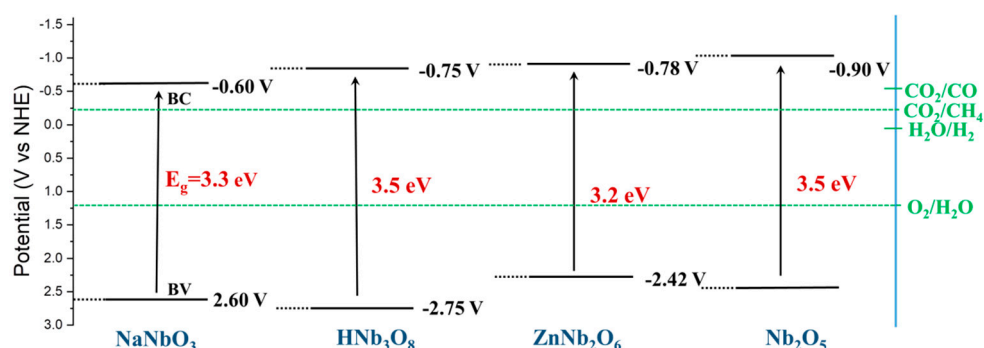| Reactions | E (V vs. RHE) |
|---|---|
| $CO_2 + 2e^- + 2H+ \rightarrow CO + H_2O$ | −0.53 |
| $CO_2 + 2e^- + 2H^+ \rightarrow HCOOH$ | −0.61 |
| $CO_2 + 4e^- + 4H^+ \rightarrow HCOH + H_2O$ | −0.48 |
| $CO_2 + 6e^- + 6H^+ \rightarrow CH_3OH + H_2O$ | −0.38 |
| $CO_2 + 8e^- + 8H^+ \rightarrow CH_4 + 2H_2O$ | −0.24 |



**Figure 13.** Band gap ($E_g$) and band positions of Nb-based semiconductors vs. normal hydrogen electrode (NHE). On the right side, the standard potentials of several redox couples are presented for comparison.

The semiconductors that have been investigated for $CO_2$ conversion present low activity, selectivity, stability, and high band gap values; therefore, challenges remain on how to make this process feasible. The $CO_2$ reduction reaction competes with $H_2$ eVolution in protic media, thus efficient catalysts must exhibit high activity for $CO_2$ conversion with low or negligible activity for $H_2$ eVolution. This requires a very high activation energy barrier for $H_2$ eVolution or a change in the reaction pathway to slow down the kinetics of $H_2$ formation [82].

Few semiconductors have been identified with high surface affinity to $CO_2$ and, simultaneously, with suitable electronic properties for $CO_2$ reduction via a photo-activated mechanism. In this sense, Nb-based materials are promising for application in $CO_2$ photoreduction owing to their properties, such as high acidity, excellent textural properties, and interesting electronic properties. Additionally, it is well-known that the product selectivity is significantly affected by the nanostructure design and the architecture of the photoactive components [83].

Efficient $CO_2$ reduction involves the optimization of synthetic procedures and the development of different architectures in order to achieve the structural, electronic, morphological, and surface properties required for this application. Despite that the application of Nb-based semiconductors for $CO_2$ photocatalytic reduction has only recently been explored, some reports have revealed the potential of these structures for artificial photosynthesis. It can be highlighted that some materials, such as alkali niobates ($NaNbO_3$ and $KNbO_3$), columbite niobates ($CuNb_2O_6$ and $ZnNb_2O_6$), niobium oxide ($Nb_2O_5$), and niobic acid ($HNb_3O_8$). Additionally, Nb-based materials have been involved in some strategies to improve the $CO_2$ photocatalytic reduction activity and selectivity, such as doping and formation of composites

Shi et al. [84] eValuated the $CO_2$ photocatalytic performance of $NaNbO_3$ with different morphologies for the first time. $NaNbO_3$ in orthorhombic phase were prepared by a conventional solid-state reaction and hydrothermal method, with micron-sized particles and homogeneous nanowires, respectively. It was observed that $NaNbO_3$ decorated with Pt was efficient to convert $CO_2$ in $CH_4$, while there was almost no $CH_4$ to be detected over pristine $NaNbO_3$. Additionally, the $CO_2$ reduction performance of Pt–$NaNbO_3$ nanowires was higher than the micron-sized particles, owing to the higher specific surface area of Pt–$NaNbO_3$ nanowires.

It is well-known that the photocatalytic reactions (oxidative or reductive processes) are particularly affected by the semiconductor crystal structure [85]. Therefore, the $CO_2$ photocatalytic reduction performance of the cubic and orthorhombic $NaNbO_3$ was eValuated. The samples were obtained using inorganic and organic Nb-precursors by a furfural alcohol-derived polymerization–oxidation [85]. Both samples exhibited the same morphology features, that is, cuboids particles with a size between 30 and 50 nm, likely owing to the use of poloxamers with surfactant behavior (Figure 14). The cubic Pt–$NaNbO_3$ presented lower band gap energy than the orthorhombic Pt–$NaNbO_3$. Cubic $NaNbO_3$ exhibited a better photocatalytic performance for $H_2$ eVolution and $CO_2$ reduction for $CH_4$ than orthorhombic $NaNbO_3$; the authors attributed this behavior to its unique electronic structure, which benefits the generation and migration of photo-generated electrons and holes. This behavior was confirmed for the same group in another publication [86]. The authors also investigated the effect of annealing temperature in the $CO_2$ reduction performance, and a deleterious effect with the increase in the temperature was observed.
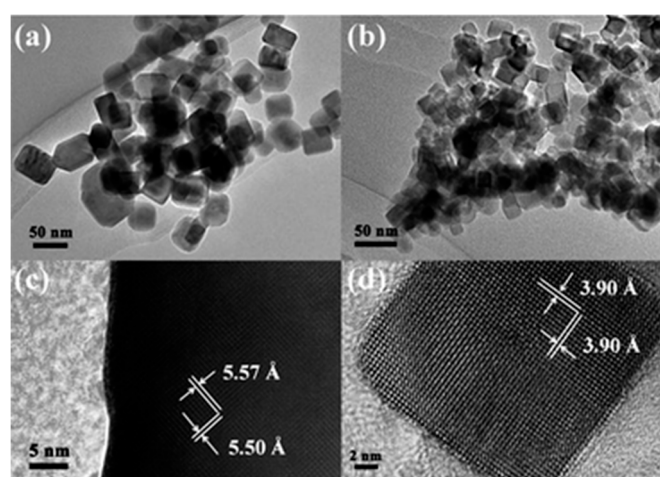


**Figure 14.** TEM images of (**a**) $NaNbO_3$–cubic and (**b**) $NaNbO_3$–orthorhombic. HR-TEM images of (**c**) $NaNbO_3$–orthorhombic and (**d**) $NaNbO_3$–cubic. Reproduced with permission from the authors of [85]. Copyright (2019), Royal Society of Chemistry, London, United Kingdom.

On the basis of previous reports, Fresno et al. eValuated the $CO_2$ photoreduction performance of $NaNbO_3$ obtained by solid state reaction at 900 °C and compared it with $NaTaO_3$ photoactivity [87]. Owing to the high annealing temperature, orthorhombic $NaNbO_3$ with low surface area was obtained

($\sim$1 m$^2 \cdot$g$^{-1}$). The main CO$_2$ reduction products were CO, CH$_4$, and CH$_3$OH, together with H$_2$ coming from the concomitant reduction of water competing with that of CO$_2$. It was observed that NaNbO$_3$ and NaTaO$_3$ give rise to similar conversions in the CO$_2$ reduction reaction. Additionally, they demonstrated that NaNbO$_3$ was photoactive eVen without a co-catalyst, although the main product was CO; the authors attributed this difference in the selectivity to the absence of a co-catalyst (Pt) [87].

Inspired in the Degussa P25, which consists of anatase and rutile TiO$_2$ (i.e., heterostructure) and shows higher activities than either pure anatase or rutile in water splitting and gaseous pollutant photodegradation [88], Ye's group proposed the investigation of heterojunction formation between NaNbO$_3$ in cubic and orthorhombic phases for the CO$_2$ photocatalytic reduction [89]. The NaNbO$_3$ samples were synthesized at 400 °C to 600 °C based on the polymerized complex method. Pure cubic and orthorhombic NaNbO$_3$ were obtained at 400 and 600 °C, respectively, while the NaNbO$_3$ samples with mixed phases were formed at the temperature ranging from 400 to 600 °C (Figure 15b,c). Along with the phase transition from the cubic phase to the orthorhombic phase, the absorption edge of NaNbO$_3$ shows a slight and gradual blue shift, which is consistent with the previous report that cubic NaNbO$_3$ has a narrower band gap than orthorhombic NaNbO$_3$ (Figure 14c). Additionally, the presence of heterojunctions between the two phases was verified; the smaller ones less than 10 nm (cubic phase) and the bigger ones about 30 nm (orthorhombic). For the CO$_2$ photocatalytic reduction experiment, Pt was used as a co-catalyst and CH$_4$ was the main product. All the mixed-phase samples were more efficient in CH$_4$ formation than the pure phases. The authors state that the photo-excited electrons migrate from the conduction band of the orthorhombic phase to the trapping sites on the cubic surface, thus avoiding the electron–hole recombination in orthorhombic NaNbO$_3$ and improving the charge separation efficiency in the mixed-phase NaNbO$_3$ samples.
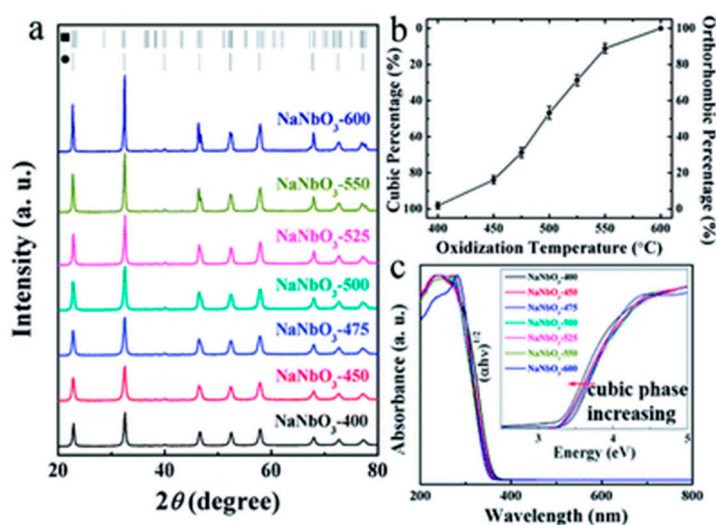


**Figure 15.** (**a**) X-ray diffraction (XRD) patterns of the as-prepared NaNbO$_3$ samples. (**b**) Dependence of cubic and orthorhombic NaNbO$_3$ contents on the annealing temperature. (**c**) UV/vis absorption spectra of the as-prepared NaNbO$_3$ samples and the inset in the figure is the corresponding ($\alpha$h$\nu$)$^{1/2}$–h$\nu$ curves. Reproduced with permission from the authors of [89]. Copyright (2019), Royal Society of Chemistry, London, United Kingdom.

Niobates materials are also efficient photocatalysts for CO$_2$ photoreduction, because a layered materials configuration is favorable for the separation and transportation of photo-excited carriers (i.e., electrons and holes) [90,91]. In this sense, niobic acid (HNb$_3$O$_8$) is a promising material, as it exhibited the valence band and the conduction band edges at desirable potential levels. The layered structure facilitates electron transfer, and the protonic acidity is favorable for water adsorption through hydrogen bonding [91]. It is expected that these properties should exert a certain positive impact on CO$_2$ photoreduction by water [91].

Therefore, Li et al. [92] eValuated the photocatalytic $CO_2$ reduction performance of $HNb_3O_8$ obtained through two different methods, hydrothermal (HT) and solid state reaction (SSR), and compared it with that of $KNb_3O_8$. $HNb_3O_8$ is isostructural with $KNb_3O_8$, and both samples were crystallized in an orthorhombic symmetry. The samples obtained through the HT method exhibited thin nanobelts with several micrometers in length, while the samples obtained by the SSR method showed containing irregular particles in micron size. The surface area value increased from 2.7 $m^2$ $g^{-1}$ of $KNb_3O_8$ (SSR) to 28.8 $m^2$ $g^{-1}$ of $KNb_3O_8$ (HT), and from 6.5 $m^2$ $g^{-1}$ of $HNb_3O_8$ (SSR) to 39.4 $m^2$ $g^{-1}$ of $HNb_3O_8$ (HT). $CH_4$ was the only one hydrocarbon product detected in the gas phase during $CO_2$ photoreduction for all samples. The rate of $CH_4$ formation over $KNb_3O_8$ (HT) was seventeen times higher than that over $KNb_3O_8$ (SSR), and the rate of $CH_4$ formation over $HNb_3O_8$ (HT) was about twenty times higher than that over $HNb_3O_8$ (SSR). Additionally, the solid acid sample ($HNb_3O_8$) exhibited higher activity than the corresponding potassium salt ($KNb_3O_8$). Also, both samples exhibited higher activity than degussa $TiO_2$–P25. Therefore, the sample morphology, specific surface area, and protonic acidity of $HNb_3O_8$ play important roles in the photocatalytic reduction of $CO_2$ to $CH_4$.

In order to improve the $CO_2$ photocatalytic reduction performance of $HNb_3O_8$, the intercalation of guest components into the interlayer space was eValuated, and lamellar $HNb_3O_8$ was purposely pillared with silica [93]. The pillarization of $HNb_3O_8$ with $SiO_2$ was verified by interlayer distance expansion, from 1.13 nm to 2.85 nm. Owing to the notably expanded interlayer distance, the surface area value of $SiO_2$-$HNb_3O_8$ was as large as 197.3 $m^2$ $g^{-1}$, in contrast to 6.5 $m^2$ $g^{-1}$ of the nonpillared $HNb_3O_8$. All of the samples were loaded with 0.4 wt% Pt by photodeposition to eValuate the $CO_2$ photoreduction. The yield of $CH_4$ over the $HNb_3O_8$ sample was almost three times higher than that achieved over $Nb_2O_5$. The improved activity for the solid acid material might be ascribed to its layered structure and the stronger adsorption ability to $H_2O$ through hydrogen bonding. The rate of $CH_4$ formation was further enhanced with the $SiO_2$-$HNb_3O_8$ sample. Additionally, the activity of the current $SiO_2$-$HNb_3O_8$ photocatalyst was higher than that of previously reported $HNb_3O_8$ nanobelts [92]. Compared with nonpillared $HNb_3O_8$, the $SiO_2$ pillared $HNb_3O_8$ sample has a notably expanded interlayer distance and much greater surface area. Thus, the reactive active sites at the interlayer space of $SiO_2$-$HNb_3O_8$ should be more accessible to the substrate. To investigate the role of protonic acidity for $CO_2$ reduction, the activity of $SiO_2$-$HNb_3O_8$ was compared with that of $SiO_2$-$KNb_3O_8$ and anatase $TiO_2$ in different molar ratios of $H_2O/CO_2$ (0.06 or 0.25). The $SiO_2$-$HNb_3O_8$ sample showed higher activity than $SiO_2$-$KNb_3O_8$ and anatase $TiO_2$; it is noteworthy that the activity of the $SiO_2$-$HNb_3O_8$ sample was more significantly enhanced than the other two samples at an elevated water content. This confirms that water molecules could react easily with the protons at the interlayer space of lamellar solid acids through hydrogen bonding.

Despite columbite niobates exhibiting interesting electronic properties and suitable conduction and valence band energies for $CO_2$ photoreduction [6], this class of material has been explored only in a limited manner. Kormányos et al. eValuated the $CO_2$ photoelectrochemical reduction activity of monoclinic type-p $CuNb_2O_6$ and orthorhombic type-n $ZnNb_2O_6$ semiconductors [94]. The $CuNb_2O_6$ and $ZnNb_2O_6$ samples showed an indirect bandgap of 1.77 eV and 3.55 eV, respectively. The photoelectrochemical (PEC) performance of the p-$CuNb_2O_6$ sample was tested in $CO_2$- and $N_2$-saturated 0.1 M $NaHCO_3$ solution. The photocurrents are two times higher (at E = −0.4 V) when the solution was saturated with $CO_2$. According to the authors, the dramatic increase in the presence of $CO_2$ is clearly attributable to the ability of $CuNb_2O_6$ to photoelectrochemically reduce $CO_2$. However, the $CuNb_2O_6$ sample's efficiency and selectivity was not eValuated, as the products formed from $CO_2$ photoelectrochemical reduction were not monitored.

Recently, da Silva et al. investigated the role of $Nb_2O_5$ surface acidity for $CO_2$ reduction performance [95]. $Nb_2O_5$ catalysts were prepared through a modified peroxide sol–gel method using different annealing temperatures, and it was verified that the increase in the annealing temperature decreases the surface acidity. The authors related the activity and selectivity of the $Nb_2O_5$ samples to their surface acidity; high surface acidity prompted the conversion of $CO_2$ to CO, HCOOH, and

$CH_3COOH$, whereas low surface acidity led to the conversion of $CO_2$ to $CH_4$. It was verified that CO is the main intermediary during the $CO_2$ photoreduction in all conditions. This work unveiled the importance of surface acidity for $CO_2$ photoreduction.

Despite the remarkable properties of $NaNbO_3$ and interesting performance for $CO_2$ photocatalytic reduction, the relative wide band gap (3.4 eV) limits its photocatalytic activity only to be active in the ultraviolet light region (4% of the solar spectrum). Therefore, there is a growing necessity to develop photocatalysts with an efficient response under visible-light irradiation. In this sense, Shi et al. design a heterostructure between $NaNbO_3$ and $C_3N_4$ in order to extended the absorption spectral range for visible region [96]. The $NaNbO_3$ sample was obtained through hydrothermal synthesis, and the heterostructure was tailored by annealing $NaNbO_3$ with melamine ($C_3N_4$ precursor) at 520 °C for 4 h. The XRD patterns of g-$C_3N_4$/$NaNbO_3$ revealed coexistence crystalline phase of $NaNbO_3$ and g-$C_3N_4$ in the composite. $NaNbO_3$ nanowires are found to randomly deposit and distribute on the surface of g-$C_3N_4$ sheets, which results in forming a heterostructured g-$C_3N_4$/$NaNbO_3$ material. The $CO_2$ photoreduction under visible irradiation showed that g-$C_3N_4$/$NaNbO_3$ improved over eight-fold the activity than that of bare $C_3N_4$ in the $CH_4$ formation. Such a remarkable enhancement of photocatalytic activity was mainly attributed to the improved separation and transfer of photogenerated electron-hole pairs at the intimate interface of g-$C_3N_4$/$NaNbO_3$ heterojunctions. The same group eValuated the $CO_2$ photoreduction performance of g-$C_3N_4$/$KNbO_3$, and the photocatalytic activity of g-$C_3N_4$/$KNbO_3$ for $CO_2$ reduction was almost four times higher than that of individual g-$C_3N_4$ under visible light irradiation [97].

Another Nb-based material that is worth mentioning is $Sr_2Bi_2Nb_2TiO_{12}$, an Aurivillius-type perovskite. Yu et al. investigated, for the first time, the $Sr_2Bi_2Nb_2TiO_{12}$ as photocatalyst for $CO_2$ photoreduction [98]. The introduction of oxygen vacancies on the surface of $Sr_2Bi_2Nb_2TiO_{12}$ extends photoresponse to cover the whole visible region and also tremendously promotes the separation of photoinduced charge carriers. Compared with the bulk material prepared by traditional solid-state reaction, the $Sr_2Bi_2Nb_2TiO_{12}$ nanosheets with the optimal oxygen vacancies concentration yields a substantially high CO eVolution rate of 17.11 μmol $g^{-1}$ $h^{-1}$.

Niobium has been used also as dopant, as it can improve the photocatalytic activities of anatase $TiO_2$ [61,99–101], by changing the crystal structure, electrical properties, and absorption characteristics of $TiO_2$. It was proposed that Nb would dope into $TiO_2$ lattice and decrease the band gap energy of the photocatalyst, and thereby Nb substitution on the Ti site creates a $Nb^{5+}$ defect state located upon the conduction band minimum. Therefore, Nb doped $TiO_2$ would work as a visible light-driven photocatalyst [61,100,101].

Nogueira et al. investigated the role of Nb-doped $TiO_2$ for $CO_2$ photocatalytic reduction to methanol [102]. The samples were obtained through the Pechini method, which promoted the substitution of $Ti^{4+}$ for $Nb^{4+}$ at different concentrations. It was observed that the surface area tends to increase with the concentration of Nb. The concentration of formed methanol was directly proportional to the Nb concentration in the $TiO_2$, the authors attributed the formation of methanol to the presence of Nb in the lattice of $TiO_2$.

The eValuation of $CO_2$ photoreduction performance of Z-scheme formed between Nb–$TiO_2$ and g-$C_3N_4$ was also eValuated [103]. It was confirmed that the band gap energy of the Nb–$TiO_2$ (2.91 eV) was lower than that of the $TiO_2$ (3.2 eV). The formation of Z-scheme Nb–$TiO_2$/g-$C_3N_4$ was eVidenced through XRD and TEM analysis. CO, $CH_4$, and $O_2$ were formed from $CO_2$ photoreduction when the Nb–$TiO_2$ sample was used. Nb–$TiO_2$/g-$C_3N_4$ not only converted $CO_2$ to CO, $CH_4$, and $O_2$, but also generated HCOOH. Additionally, 50Nb–$TiO_2$/50g-$C_3N_4$ was the best material for the $CO_2$ reduction.

It is well known that, while metals and semiconductors usually exhibit great stability, but poor selectivity for $CO_2$ reduction, enzymes and metal complexes can selectively convert $CO_2$ into CO, but they lack long-term stability. Therefore, Faustino et al. eValuated the role of hexaniobate nanoscrolls ($K_xH_{(4-x)}Nb_6O_{17}$) as suitable substrates for the immobilization of two kinds of Re(I)-based molecular catalysts (namely I and II) for $CO_2$ photoreduction [104]. Hexaniobate nanoscrolls were obtained

through solid state reaction with subsequent proton exchange and exfoliation with *tert*-butylammonium hydroxide. The Re(I) complexes were immobilized by an adsorption process that was verified for UV/vis absorption and Fourier-transform infrared (FTIR) spectroscopies. As a result of the hexaniobate exfoliation, the specific surface area was increased from 2 $m^2$ $g^{-1}$ to 110 $m^2$ $g^{-1}$. The sensitized oxides were employed as visible-light photocatalysts for $CO_2$ reduction in 5:1 dimethylformamide (DMF)/TEOA exposed to a 300 W Xe lamp ($\lambda = 420$ nm). The possible gaseous products were analyzed by mass spectrometry with CO being the only detected photoproduct. The complexes immobilized on the surfaces of the oxides exhibited much higher turnover number ($TON_{CO}$) than those in solution. For comparative purposes, the complexes were immobilized on $TiO_2$ as well. While for complex I, the immobilization on the niobate nanoscrolls led to 20% higher $TON_{CO}$ in comparison with that observed on $TiO_2$, for complex II, the opposite behavior was observed; that is, the immobilization on $TiO_2$ led to better photoactivities. Such behavior was rationalized based on the recombination kinetics of each composite and on the reductive potential of the injected electrons on the niobate or $TiO_2$ conduction bands. For comparison, a summary of the photoactivity of Nb-based photocatalysts towards $CO_2$ reduction is presented in Table 4.

**Table 4.** Summary of the photocatalytic activity of Nb-based compounds combined with distinct materials towards $CO_2$ reduction.

| Nb-Based Material | Co-Catalyst | Light Source | Main Products | Observed Rate | Ref. |
|---|---|---|---|---|---|
| $NaNbO_3$ | Pt | 300 W Xe | $CH_4$ | 653 ppm $h^{-1}$ $g^{-1}$ | [84] |
| $NaNbO_3$ | Pt | 300 W Xe > 300 nm | $CH_4$ | 10.4 µmol $h^{-1}$ $m^{-2}$ | [85] |
| $NaNbO_3$ | None | 300 W Xe > 420 nm | CO, $CH_4$, $CH_3OH$, $H_2$ | NA | [87] |
| $NaNbO_3$ heterojunction | Pt | 300 W Xe > 300 nm | $CH_4$ | ~10 µmol $h^{-1}$ $m^{-2}$ | [89] |
| $HNb_3O_8$ | None | 350 W Xe | $CH_4$ | 3.5 µmol $g^{-1}$ $h^{-1}$ | [92] |
| $SiO_2$-Pillared $HNb_3O_8$ | Pt | 350 W Xe | $CH_4$ | 2.90 µmol $g^{-1}$ $h^{-1}$ | [93] |
| $Nb_2O_5$ | None | UVC lamp, 0.167 mW $cm^{-2}$ | CO, $CH_4$, $CH_3COOH$, HCOOH | ~10 µmol $L^{-1}$ $g^{-1}$ | [95] |
| $C_3N_4/NaNbO_3$ | None | 300 W Xe $\lambda > 420$ nm | $CH_4$ | ~6 µmol $h^{-1}$ $g^{-1}$ | [96] |
| $C_3N_4/KNbO_3$ | Pt | 300 W Xe $\lambda > 420$ nm | $CH_4$ | 0.25 µmol $h^{-1}$ | [97] |
| Re(I) polypyridyl complexes/$K_xH_{4-x}Nb_6O_{17}$ | None | 300 W Xe $\lambda > 420$ nm | CO | 2.9 * | [104] |

\* Turnover frequency (TOF), $h^{-1}$.

## 4. Concluding Remarks and Perspectives

Over the past few years, great efforts have been spent by the scientific community to develop clean renewable energy sources. Photocatalysis can be described as an efficient method to produce solar fuels from available sources as $H_2O$ and $CO_2$. Nevertheless, it is always a challenge to develop efficient materials able to promote solar-to-fuel conversion. In this sense, niobium-based materials offer diverse possibilities to engineer compounds showing important characteristics for photocatalytic processes such as efficient light absorption, charge separation, and charge transfer reaction. Herein, we could provide a glimpse from the last years on the extensive flexibility offered by niobium-based compounds for $CO_2$ reduction and notably for $H_2$ eVolution. Niobium oxides as $Nb_2O_5$ and the wide range of niobates offer untold possibilities of structure, morphologies, and electronic configuration, which can supply desired properties for photocatalytic reactions. Moreover, niobium cations as a dopant have provided the opportunity to tune band energy positions and increase the efficient of other materials. Thus, niobium-based compounds are promising materials that still offer opportunities of new investigations and insights regarding photocatalytic applications.

**Conflicts of Interest:** The authors declare no conflict of interest.

## References

1. BP Statistical Review of World Energy. Available online: https://www.bp.com/content/dam/bp/business-sites/en/global/corporate/pdfs/energy-economics/statistical-review/bp-stats-review-2019-full-report.pdf (accessed on 13 November 2019).
2. Christoforidis, K.C.; Fornasiero, P. Photocatalysis for Hydrogen Production and $CO_2$ Reduction: The Case of Copper-Catalysts. *ChemCatChem* **2019**, *11*, 368–382. [CrossRef]
3. Li, K.; Peng, B.; Peng, T.Y. Recent Advances in Heterogeneous Photocatalytic $CO_2$ Conversion to Solar Fuels. *ACS Catal.* **2016**, *6*, 7485–7527. [CrossRef]
4. Kim, J.H.; Hansora, D.; Sharma, P.; Jang, J.W.; Lee, J.S. Toward practical solar hydrogen production—An artificial photosynthetic leaf-to-farm challenge. *Chem. Soc. Rev.* **2019**, *48*, 1908–1971. [CrossRef] [PubMed]
5. Fujishima, A.; Honda, K. Electrochemical Photolysis of Water at a Semiconductor Electrode. *Nature* **1972**, *238*, 38–40. [CrossRef] [PubMed]
6. Nico, C.; Monteiro, T.; Graça, M.P.F. Niobium oxides and niobates physical properties: Review and prospects. *Prog. Mater. Sci.* **2016**, *80*, 1–37. [CrossRef]
7. Lopes, O.F.; de Mendonça, V.R.; Silva, F.B.F.; Paris, E.C.; Ribeiro, C. Niobium oxides: An overview of the synthesis of $Nb_2O_5$ and its application in heterogeneous photocatalysis. *Quim. Nova* **2014**, *38*, 106–117. [CrossRef]
8. Nunes, B.N.; Faustino, L.A.; Muller, A.V.; Polo, A.S.; Patrocinio, A.O.T. $Nb_2O_5$ dye-sensitized solar cells. In *Nanomaterials for Solar Cell Application*, 2nd ed.; Thomas, S., Sakho, E.H.M., Kalarikkal, N., Oluwafemi, S.O., Wu, J., Eds.; Elsevier: Oxford, UK, 2019; pp. 287–322.
9. Nowak, I.; Ziolek, M. Niobium Compounds: Preparation, Characterization, and Application in Heterogeneous Catalysis. *Chem. Rev.* **1999**, *99*, 3603–3624. [CrossRef]
10. Ziolek, M. Niobium-containing catalysts—The state of the art. *Catal. Today* **2003**, *78*, 47–64. [CrossRef]
11. Bizeto, M.A.; Shiguihara, A.L.; Constantino, V.R.L. Layered niobate nanosheets: Building blocks for advanced materials assembly. *J. Mater. Chem.* **2009**, *19*, 2512–2525. [CrossRef]
12. Sarahan, M.C.; Carroll, E.C.; Allen, M.; Larsen, D.S.; Browning, N.D.; Osterloh, F.E. $K_4Nb_6O_{17}$-derived photocatalysts for hydrogen eVolution from water: Nanoscrolls versus nanosheets. *J. Solid State Chem.* **2008**, *181*, 1678–1683. [CrossRef]
13. Ebina, Y.; Sasaki, T.; Watanabe, M. Study on exfoliation of layered perovskite-type niobates. *Solid State Ion.* **2002**, *151*, 177–182. [CrossRef]
14. Shiguihara, A.L.; Bizeto, M.A.; Constantino, V.R.L. Exfoliation of layered hexaniobate in tetra(n-butyl)ammonium hydroxide aqueous solution. *Colloids Surf. A Physicochem. Eng. Asp.* **2007**, *295*, 123–129. [CrossRef]
15. Ravishankar, T.N.; Vaz, M.d.O.; Ramakrishnappa, T.; Teixeira, S.R.; Dupont, J. Ionic liquid–assisted hydrothermal synthesis of $Nb/TiO_2$ nanocomposites for efficient photocatalytic hydrogen production and photodecolorization of Rhodamine B under UV-visible and visible light illuminations. *Mater. Today Chem.* **2019**, *12*, 373–385. [CrossRef]
16. Yang, M.; Kim, D.; Jha, H.; Lee, K.; Paul, J.; Schmuki, P. Nb doping of $TiO_2$ nanotubes for an enhanced efficiency of dye-sensitized solar cells. *Chem. Commun.* **2011**, *47*, 2032–2034. [CrossRef]
17. Emeline, A.V.; Furubayashi, Y.; Zhang, X.; Jin, M.; Murakami, T.; Fujishima, A. Photoelectrochemical behavior of Nb-doped $TiO_2$ electrodes. *J. Phys. Chem. B* **2005**, *109*, 24441–24444. [CrossRef]
18. Singh, R.; Ryu, I.; Yadav, H.; Park, J.; Jo, J.W.; Yim, S.; Lee, J.J. Non-hydrolytic sol-gel route to synthesize $TiO_2$ nanoparticles under ambient condition for highly efficient and stable perovskite solar cells. *Sol. Energy* **2019**, *185*, 307–314. [CrossRef]

19. El-Shazly, T.S.; Hassan, W.M.I.; Abdel Rahim, S.T.; Allam, N.K. Unravelling the interplay of dopant concentration and band structure engineering of monoclinic niobium pentoxide: A model photoanode for water splitting. *Int. J. Hydrogen Energy* **2015**, *40*, 13867–13875. [CrossRef]

20. Kulkarni, A.K.; Praveen, C.S.; Sethi, Y.A.; Panmand, R.P.; Arbuj, S.S.; Naik, S.D.; Ghule, A.V.; Kale, B.B. Nanostructured N-doped orthorhombic $Nb_2O_5$ as an efficient stable photocatalyst for hydrogen generation under visible light. *Dalton Trans.* **2017**, *46*, 14859–14868. [CrossRef]

21. Huang, Q.Z.; Wang, J.C.; Wang, P.P.; Yao, H.C.; Li, Z.J. In-situ growth of mesoporous $Nb_2O_5$ microspheres on g-$C_3N_4$ nanosheets for enhanced photocatalytic $H_2$ eVolution under visible light irradiation. *Int. J. Hydrogen Energy* **2017**, *42*, 6683–6694. [CrossRef]

22. Wen, P.H.; Ai, L.L.; Liu, T.T.; Hu, D.W.; Yao, F.Y. Hydrothermal topological synthesis and photocatalyst performance of orthorhombic $Nb_2O_5$ rectangle nanosheet crystals with dominantly exposed (010) facet. *Mater. Des.* **2017**, *117*, 346–352. [CrossRef]

23. Wen, P.H.; Ai, L.L.; Wei, F.Y.; Hu, D.W.; Guo, J.J.; Yao, F.Y.; Liu, T.T. In-situ synthesis of crystalline Ag-$Nb_2O_5$ nanobelt clusters with enhanced solar photo-electrochemical performance for splitting water. *Mater. Des.* **2017**, *131*, 219–225. [CrossRef]

24. Zhou, C.; Shi, R.; Yang, G.; Meng, X.; Wu, L.Z.; Tung, C.H.; Zhang, T. Spatial separation of charge carriers in $Nb_2O_5$ nanorod superstructures for enhanced photocatalytic $H_2$ production activity. *Mater. Today Chem.* **2018**, *10*, 259–263. [CrossRef]

25. Zhang, Y.; Zhao, H.; Zhao, X.F.; Lin, J.N.; Li, N.; Huo, Z.Y.; Yan, Z.F.; Zhang, M.; Hu, S. Narrow-bandgap $Nb_2O_5$ nanowires with enclosed pores as high-performance photocatalyst. *Sci. China Mater.* **2019**, *62*, 203–210. [CrossRef]

26. Kumar, A.; Islam, R.; Pramanik, D.; Saraswat, K. On the limit of defect doping in transition metal oxides. *J. Vac. Sci. Technol. A* **2019**, *37*. [CrossRef]

27. Zhao, W.L.; Zhao, W.; Zhu, G.L.; Lin, T.Q.; Xu, F.F.; Huang, F.Q. Black $Nb_2O_5$ nanorods with improved solar absorption and enhanced photocatalytic activity. *Dalton Trans.* **2016**, *45*, 3888–3894. [CrossRef] [PubMed]

28. Huang, H.; Zhou, J.; Zhou, J.; Zhu, M.S. Structure-retentive synthesis of a highly ordered mesoporous $Nb_2O_5$/N-doped graphene nanocomposite with superior interfacial contacts and improved visible-light photocatalysis. *Catal. Sci. Technol.* **2019**, *9*, 3373–3379. [CrossRef]

29. Khan, I.; Baig, N.; Qurashi, A. Graphitic carbon nitride impregnated niobium oxide (g-$C_3N_4$/$Nb_2O_5$) type (II) heterojunctions and its synergetic solar-driven hydrogen generation. *ACS Appl. Energy Mater.* **2019**, *2*, 607–615. [CrossRef]

30. Idrees, F.; Dillert, R.; Bahnemann, D.; Butt, F.; Tahir, M. In-Situ Synthesis of $Nb_2O_5$/g-$C_3N_4$ Heterostructures as Highly Efficient Photocatalysts for Molecular $H_2$ eVolution under Solar Illumination. *Catalysts* **2019**, *9*, 169. [CrossRef]

31. Nunes, B.N.; Patrocinio, A.O.T.; Bahnemann, D.W. Influence of the preparation conditions on the morphology and photocatalytic performance Pt-modified hexaniobate composites. *J. Phys. Condens. Matter* **2019**, *31*, 394001. [CrossRef]

32. Reisman, A.; Holtzberg, F. Phase Equilibria in the System $K_2CO_3$-$Nb_2O_5$ by the Method of Differential Thermal Analysis. *J. Am. Chem. Soc.* **1955**, *77*, 2115–2119. [CrossRef]

33. Nassau, K.; Shiever, J.W.; Bernstein, J.L. Crystal Growth and Properties of Nica-Like Potassium Niobates. *J. Electrochem. Soc.* **1969**, *116*, 348–353. [CrossRef]

34. Dion, M.; Ganne, M.; Tournoux, M. Nouvelles familles de phases $MIMII_2Nb_3O_{10}$ a feuillets "perovskites". *Mater. Res. Bull.* **1981**, *16*, 1429–1435. [CrossRef]

35. Jacobson, A.J.; Johnson, J.W.; Lewandowski, J.T. Interlayer Chemistry between Thick Transition-Metal Oxide Layers: Synthesis and Intercalation Reactions of K[$Ca_2Na_{n-3}Nb_nO_{3n+1}$] ($3 \leq n \leq 7$). *Inorg. Chem.* **1985**, *24*, 3727–3729. [CrossRef]

36. Nunes, B.N.; Haisch, C.; Emeline, A.V.; Bahnemann, D.W.; Patrocinio, A.O.T. Photocatalytic properties of layer-by-layer thin films of hexaniobate nanoscrolls. *Catal. Today* **2019**, *326*, 60–67. [CrossRef]

37. Oshima, T.; Lu, D.; Maeda, K. Preparation of Pt-Intercalated $KCa_2Nb_3O_{10}$ Nanosheets and Their Photocatalytic Activity for Overall Water Splitting. *ChemNanoMat* **2016**, *2*, 748–755. [CrossRef]

38. Kulischow, N.; Ladasiu, C.; Marschall, R. Layered Dion-Jacobson type niobium oxides for photocatalytic hydrogen production prepared via molten salt synthesis. *Catal. Today* **2017**, *287*, 65–69. [CrossRef]

39. Zhou, Y.N.; Wen, T.; Guo, Y.Z.; Yang, B.C.; Wang, Y.G. Controllable doping of nitrogen and tetravalent niobium affords yellow and black calcium niobate nanosheets for enhanced photocatalytic hydrogen eVolution. *RSC Adv.* **2016**, *6*, 64930–64936. [CrossRef]

40. Zhou, Y.N.; Wen, T.; Zhang, X.F.; Chang, B.B.; Kong, W.Q.; Guo, Y.Z.; Yang, B.C.; Wang, Y.G. A Multiple Structure-Design Strategy towards Ultrathin Niobate Perovskite Nanosheets with Thickness-Dependent Photocatalytic Hydrogen-Evolution Performance. *Chem. Asian J.* **2017**, *12*, 2727–2733. [CrossRef] [PubMed]

41. Xiong, J.H.; Jing, K.Q.; Zou, J.H.; Liang, S.J.; Wu, L. A hybrid of CdS/HCa$_2$Nb$_3$O$_{10}$ ultrathin nanosheets for promoting photocatalytic hydrogen eVolution. *Dalton Trans.* **2017**, *46*, 13935–13942. [CrossRef] [PubMed]

42. Hu, Y.C.; Li, G.S.; Zong, S.C.; Shi, J.W.; Guo, L.J. Self-assembled nanohybrid of cadmium sulfide and calcium niobate: Photocatalyst with enhanced charge separation for efficient visible light induced hydrogen generation. *Catal. Today* **2018**, *315*, 117–125. [CrossRef]

43. Xiong, J.H.; Liu, Y.H.; Liang, S.J.; Zhang, S.Y.; Li, Y.H.; Wu, L. Insights into the role of Cu in promoting photocatalytic hydrogen production over ultrathin HNb$_3$O$_8$ nanosheets. *J. Catal.* **2016**, *342*, 98–104. [CrossRef]

44. Xia, Y.Z.; Liang, S.J.; Wu, L.; Wang, X.X. Ultrasmall NiS decorated HNb$_3$O$_8$ nanosheeets as highly efficient photocatalyst for H$_2$ eVolution reaction. *Catal. Today* **2019**, *330*, 195–202. [CrossRef]

45. Wang, J.J.; Teng, J.; Pu, L.Z.; Huang, J.; Wang, Y.; Li, Q.X. Double-hole-mediated coupling of anionic dopants in perovskite NaNbO$_3$ for efficient solar water splitting. *Int. J. Quantum Chem.* **2019**, *119*, e25930. [CrossRef]

46. Kaneko, M.; Mishima, K.; Yamashita, K. First-principles study on visible light absorption of defected SrNbO$_3$. *J. Photochem. Photobiol. A Chem.* **2019**, *375*, 175–180. [CrossRef]

47. Yu, J.X.; Chen, Z.Q.; Chen, Q.Q.; Wang, Y.; Lin, H.J.; Hu, X.; Zhao, L.H.; He, Y.M. Giant enhancement of photocatalytic H$_2$ production over KNbO$_3$ photocatalyst obtained via carbon doping and MoS$_2$ decoration. *Int. J. Hydrogen Energy* **2018**, *43*, 4347–4354. [CrossRef]

48. Huang, S.S.; Lang, J.Y.; Du, C.F.; Bian, F.G.; Su, Y.G.; Wang, X.J. Enhanced driving force and charge separation efficiency in disordered SnNb$_x$O$_y$: Boosting photocatalytic activity toward water reduction. *Chem. Eng. J.* **2017**, *309*, 313–320. [CrossRef]

49. Kamimura, S.; Abe, S.; Tsubota, T.; Ohno, T. Solar-driven H$_2$ eVolution over CuNb$_2$O$_6$: Effect of two polymorphs (monoclinic and orthorhombic) on optical property and photocatalytic activity. *J. Photochem. Photobiol. A Chem.* **2018**, *356*, 263–271. [CrossRef]

50. Chun, Y.T.; Yue, M.F.; Jiang, P.F.; Chen, S.J.; Gao, W.L.; Cong, R.H.; Yang, T. Optimizing the performance of photocatalytic H$_2$ generation for ZnNb$_2$O$_6$ synthesized by a two-step hydrothermal method. *RSC Adv.* **2018**, *8*, 13857–13864. [CrossRef]

51. Betzler, S.B.; Podjaski, F.; Beetz, M.; Handloser, K.; Wisnet, A.; Handloser, M.; Hartschuh, A.; Lotsch, B.V.; Scheu, C. Titanium Doping and Its Effect on the Morphology of Three-Dimensional Hierarchical Nb$_3$O$_7$(OH) Nanostructures for Enhanced Light-Induced Water Splitting. *Chem. Mater.* **2016**, *28*, 7666–7672. [CrossRef]

52. Zhang, B.; Hui, D.P.; Li, Y.X.; Zhao, H.; Wang, C.Y. Synthesis and photocatalytic hydrogen production activity of the Ni-CH$_3$CH$_2$NH$_2$/H$_{1.78}$Sr$_{0.78}$Bi$_{0.22}$Nb$_2$O$_7$ hybrid layered perovskite. *Chin. J. Catal.* **2017**, *38*, 2039–2047. [CrossRef]

53. Grodziuk, G.Y.; Shcherban, N.D.; Shvalagin, V.V.; Korzhak, A.V.; Andryushina, N.S.; Skoryk, M.A.; Kuchmiy, S.Y. Photocatalytic activity of nanostructured composites based on layered niobates and C$_3$N$_4$ in the hydrogen eVolution reaction from electron donor solutions under visible light. *Int. J. Hydrogen Energy* **2017**, *42*, 24108–24116. [CrossRef]

54. Thaweesak, S.; Lyu, M.; Peerakiatkhajohn, P.; Butburee, T.; Luo, B.; Chen, H.J.; Wang, L.Z. Two-dimensional g-C$_3$N$_4$/Ca$_2$Nb$_2$TaO$_{10}$ nanosheet composites for efficient visible light photocatalytic hydrogen eVolution. *Appl. Catal. B Environ.* **2017**, *202*, 184–190. [CrossRef]

55. Wang, K.; Li, Y.; Li, J.; Zhang, G. Boosting interfacial charge separation of Ba$_5$Nb$_4$O$_{15}$/g-C$_3$N$_4$ photocatalysts by 2D/2D nanojunction towards efficient visible-light driven H$_2$ generation. *Appl. Catal. B Environ.* **2019**, *263*, 117730. [CrossRef]

56. Chen, P.F.; Xing, P.X.; Chen, Z.Q.; Hu, X.; Lin, H.J.; Zhao, L.H.; He, Y.M. In-situ synthesis of AgNbO$_3$/g-C$_3$N$_4$ photocatalyst via microwave heating method for efficiently photocatalytic H$_2$ generation. *J. Colloid Interface Sci.* **2019**, *534*, 163–171. [CrossRef] [PubMed]

57. Chen, Z.Q.; Chen, P.F.; Xing, P.X.; Hu, X.; Lin, H.J.; Wu, Y.; Zhao, L.H.; He, Y.M. Rapid fabrication of KTa$_{0.75}$Nb$_{0.25}$/g-C$_3$N$_4$ composite via microwave heating for efficient photocatalytic H$_2$ eVolution. *Fuel* **2019**, *241*, 1–11. [CrossRef]

58. Fujito, H.; Kunioku, H.; Kato, D.; Suzuki, H.; Higashi, M.; Kageyama, H.; Abe, R. Layered Perovskite Oxychloride $Bi_4NbO_8Cl$: A Stable Visible Light Responsive Photocatalyst for Water Splitting. *J. Am. Chem. Soc.* **2016**, *138*, 2082–2085. [CrossRef]

59. Wakayama, H.; Hibino, K.; Fujii, K.; Oshima, T.; Yanagisawa, K.; Kobayashi, Y.; Kimoto, K.; Yashima, M.; Maeda, K. Synthesis of a Layered Niobium Oxynitride, $Rb_2NdNb_2O_6NH_2O$, Showing Visible-Light Photocatalytic Activity for $H_2$ eVolution. *Inorg. Chem.* **2019**, *58*, 6161–6166. [CrossRef]

60. Tian, Z.L.; Cui, H.L.; Xu, J.J.; Zhu, G.L.; Shao, F.; He, J.Q.; Huang, F.Q. Efficient Charge Separation of In-Situ Nb-Doped $TiO_2$ Nanowires for Photoelectrochemical Water–splitting. *ChemistrySelect* **2017**, *2*, 2822–2827. [CrossRef]

61. Kong, L.; Wang, C.H.; Zheng, H.; Zhang, X.T.; Liu, Y.C. Defect-Induced Yellow Color in Nb-Doped $TiO_2$ and Its Impact on Visible-Light Photocatalysis. *J. Phys. Chem. C* **2015**, *119*, 16623–16632. [CrossRef]

62. Caudillo-Flores, U.; Muñoz-Batista, M.J.; Cortés, J.A.; Fernández-García, M.; Kubacka, A. UV and visible light driven $H_2$ photo-production using Nb-doped $TiO_2$: Comparing Pt and Pd co-catalysts. *Mol. Catal.* **2017**, *437*, 1–10. [CrossRef]

63. Flores, E.; Ares, J.R.; Sánchez, C.; Ferrer, I.J. Ternary transition titanium-niobium trisulfide as photoanode for assisted water splitting. *Catal. Today* **2019**, *321–322*, 107–112. [CrossRef]

64. Zoellner, B.; O'Donnell, S.; Wu, Z.; Itanze, D.; Carbone, A.; Osterloh, F.E.; Geyer, S.; Maggard, P.A. Impact of Nb(V) Substitution on the Structure and Optical and Photoelectrochemical Properties of the $Cu_5(Ta_{1−x}Nb_x)_{11}O_{30}$ Solid Solution. *Inorg. Chem.* **2019**, *58*, 6845–6857. [CrossRef] [PubMed]

65. Thanh Truc, N.T.; Tran, D.T.; Hanh, N.T.; Pham, T.D. Novel visible light-driven Nb-doped $Ta_3N_5$ sensitized/protected by PPy for efficient overall water splitting. *Int. J. Hydrogen Energy* **2018**, *43*, 15898–15906. [CrossRef]

66. Chen, Z.Q.; Chen, P.F.; Xing, P.X.; Hu, X.; Lin, H.J.; Wu, Y.; Zhao, L.H.; He, Y.M. Novel carbon modified $KTa_{0.75}Nb_{0.25}O_3$ nanocubes with excellent efficiency in photocatalytic $H_2$ eVolution. *Fuel* **2018**, *233*, 486–496. [CrossRef]

67. Monfort, O.; Sfaelou, S.; Satrapinskyy, L.; Plecenik, T.; Roch, T.; Plesch, G.; Lianos, P. Comparative study between pristine and Nb-modified $BiVO_4$ films employed for photoelectrocatalytic production of $H_2$ by water splitting and for photocatalytic degradation of organic pollutants under simulated solar light. *Catal. Today* **2017**, *280*, 51–57. [CrossRef]

68. Fontelles-Carceller, O.; Muñoz-Batista, M.J.; Conesa, J.C.; Kubacka, A.; Fernández-García, M. $H_2$ photo-production from methanol, ethanol and 2-propanol: Pt-(Nb)$TiO_2$ performance under UV and visible light. *Mol. Catal.* **2018**, *446*, 88–97. [CrossRef]

69. Kalanur, S.S.; Yoo, I.H.; Cho, I.S.; Seo, H. Niobium incorporated $WO_3$ nanotriangles: Band edge insights and improved photoelectrochemical water splitting activity. *Ceram. Int.* **2019**, *45*, 8157–8165. [CrossRef]

70. Patel, P.P.; Hanumantha, P.J.; Velikokhatnyi, O.I.; Datta, M.K.; Gattu, B.; Poston, J.A.; Manivannan, A.; Kumta, P.N. Vertically aligned nitrogen doped (Sn,Nb)$O_2$ nanotubes—Robust photoanodes for hydrogen generation by photoelectrochemical water splitting. *Mater. Sci. Eng. B Solid State Mater. Adv. Technol.* **2016**, *208*, 1–14. [CrossRef]

71. IPCC The Intergovernmental Panel on Climate Change. Available online: http://www.ipcc.ch/ (accessed on 20 November 2019).

72. Lim, C.H.; Holder, A.M.; Hynes, J.T.; Musgrave, C.B. Catalytic Reduction of $CO_2$ by Renewable Organohydrides. *J. Phys. Chem. Lett.* **2015**, *6*, 5078–5092. [CrossRef]

73. Mondal, B.; Song, J.; Neese, F.; Ye, S. Bio-inspired mechanistic insights into $CO_2$ reduction. *Curr. Opin. Chem. Biol.* **2015**, *25*, 103–109. [CrossRef]

74. Mao, Z.Y.; Chen, J.J.; Yang, Y.F.; Wang, D.J.; Bie, L.J.; Fahlman, B.D. Novel g-$C_3N_4$/CoO Nanocomposites with Significantly Enhanced Visible-Light Photocatalytic Activity for $H_2$ eVolution. *ACS Appl. Mater. Interfaces* **2017**, *9*, 12427–12435. [CrossRef]

75. Gutierrez-Guerra, N.; Moreno-Lopez, L.; Serrano-Ruiz, J.C.; Valverde, J.L.; de Lucas-Consuegra, A. Gas phase electrocatalytic conversion of $CO_2$ to syn-fuels on Cu based catalysts-electrodes. *Appl. Catal. B Environ.* **2016**, *188*, 272–282. [CrossRef]

76. Ciamician, G. The Photochemistry of the Future. *Science* **1912**, *36*, 385–394. [CrossRef] [PubMed]

77. Inoue, T.; Fujishima, A.; Konishi, S.; Honda, K. Photoelectrocatalytic reduction of carbon dioxide in aqueous suspensions of semiconductor powders. *Nature* **1979**, *277*, 637–638. [CrossRef]

78. D'Alessandro, D.M.; Smit, B.; Long, J.R. Carbon dioxide capture: Prospects for new materials. *Angew. Chem. Int. Ed.* **2010**, *49*, 6058–6082. [CrossRef] [PubMed]

79. Kauffman, D.R.; Thakkar, J.; Siva, R.; Matranga, C.; Ohodnicki, P.R.; Zeng, C.; Jin, R. Efficient Electrochemical $CO_2$ Conversion Powered by Renewable Energy. *ACS Appl. Mater. Interfaces* **2015**, *7*, 15626–15632. [CrossRef] [PubMed]

80. Hsieh, Y.C.; Senanayake, S.D.; Zhang, Y.; Xu, W.Q.; Polyansky, D.E. Effect of Chloride Anions on the Synthesis and Enhanced Catalytic Activity of Silver Nanocoral Electrodes for $CO_2$ Electroreduction. *ACS Catal.* **2015**, 5349–5356. [CrossRef]

81. Kortlever, R.; Shen, J.; Schouten, K.J.P.; Calle-Vallejo, F.; Koper, M.T.M. Catalysts and Reaction Pathways for the Electrochemical Reduction of Carbon Dioxide. *J. Phys. Chem. Lett.* **2015**, *6*, 4073–4082. [CrossRef]

82. Ma, Y.; Wang, X.L.; Jia, Y.S.; Chen, X.B.; Han, H.X.; Li, C. Titanium dioxide-based nanomaterials for photocatalytic fuel generations. *Chem. Rev.* **2014**, *114*, 9987–10043. [CrossRef]

83. Ong, W.J.; Tan, L.L.; Ng, Y.H.; Yong, S.T.; Chai, S.P. Graphitic Carbon Nitride (g-$C_3N_4$)-Based Photocatalysts for Artificial Photosynthesis and Environmental Remediation: Are We a Step Closer To Achieving Sustainability? *Chem. Rev.* **2016**, *116*, 7159–7329. [CrossRef]

84. Shi, H.F.; Wang, T.Z.; Chen, J.; Zhu, C.; Ye, J.H.; Zou, Z.G. Photoreduction of carbon dioxide over $NaNbO_3$ nanostructured photocatalysts. *Catal. Lett.* **2011**, *141*, 525–530. [CrossRef]

85. Li, P.; Ouyang, S.; Zhang, Y.J.; Kako, T.; Ye, J.H. Surface-coordination-induced selective synthesis of cubic and orthorhombic $NaNbO_3$ and their photocatalytic properties. *J. Mater. Chem. A* **2013**, *1*, 1185–1191. [CrossRef]

86. Li, P.; Ouyang, S.; Xi, G.C.; Kako, T.; Ye, J.H. The Effects of Crystal Structure and Electronic Structure on Photocatalytic $H_2$ eVolution and $CO_2$ Reduction over Two Phases of Perovskite-Structured $NaNbO_3$. *J. Phys. Chem. C* **2012**, *116*, 7621–7628. [CrossRef]

87. Fresno, F.; Jana, P.; Reñones, P.; Coronado, J.M.; Serrano, D.P.; De La Peña O'Shea, V.A. $CO_2$ reduction over $NaNbO_3$ and $NaTaO_3$ perovskite photocatalysts. *Photochem. Photobiol. Sci.* **2017**, *16*, 17–23. [CrossRef] [PubMed]

88. Ohno, T.; Sarukawa, K.; Tokieda, K.; Matsumura, M. Morphology of a $TiO_2$ Photocatalyst (Degussa, P-25) Consisting of Anatase and Rutile Crystalline Phases. *J. Catal.* **2001**, *86*, 82–86. [CrossRef]

89. Li, P.; Xu, H.; Liu, L.Q.; Kako, T.; Umezawa, N.; Abe, H.; Ye, J.H. Constructing cubic-orthorhombic surface-phase junctions of $NaNbO_3$ towards significant enhancement of $CO_2$ photoreduction. *J. Mater. Chem. A* **2014**, *2*, 5606–5609. [CrossRef]

90. Low, J.X.; Cao, S.W.; Yu, J.G.; Wageh, S. Two-dimensional layered composite photocatalysts. *Chem. Commun.* **2014**, *50*, 10768–10777. [CrossRef]

91. Li, X.K.; Kikugawa, N.; Ye, J.H. Nitrogen-doped lamellar niobic acid with visible light-responsive photocatalytic activity. *Adv. Mater.* **2008**, *20*, 3816–3819. [CrossRef]

92. Li, X.K.; Pan, H.Q.; Li, W.; Zhuang, Z.J. Photocatalytic reduction of $CO_2$ to methane over $HNb_3O_8$ nanobelts. *Appl. Catal. A Gen.* **2012**, *413–414*, 103–108. [CrossRef]

93. Li, X.K.; Li, W.; Zhuang, Z.J.; Zhong, Y.S.; Li, Q.; Wang, L.Y. Photocatalytic Reduction of Carbon Dioxide to Methane over $SiO_2$-Pillared $HNb_3O_8$. *J. Phys. Chem. C* **2012**, *116*, 16047–16053. [CrossRef]

94. Kormányos, A.; Thomas, A.; Huda, M.N.; Sarker, P.; Liu, J.P.; Poudyal, N.; Janáky, C.; Rajeshwar, K. Solution Combustion Synthesis, Characterization, and Photoelectrochemistry of $CuNb_2O_6$ and $ZnNb_2O_6$ Nanoparticles. *J. Phys. Chem. C* **2016**, *120*, 16024–16034. [CrossRef]

95. da Silva, G.T.S.T.; Nogueira, A.E.; Oliveira, J.A.; Torres, J.A.; Lopes, O.F.; Ribeiro, C. Acidic surface niobium pentoxide is catalytic active for $CO_2$ photoreduction. *Appl. Catal. B Environ.* **2019**, *242*, 349–357. [CrossRef]

96. Shi, H.F.; Chen, G.Q.; Zhang, C.L.; Zou, Z.G. Polymeric g-$C_3N_4$ coupled with $NaNbO_3$ nanowires toward enhanced photocatalytic reduction of $CO_2$ into renewable fuel. *ACS Catal.* **2014**, *4*, 3637–3643. [CrossRef]

97. Shi, H.F.; Zhang, C.L.; Zhou, C.P.; Chen, G.Q. Conversion of $CO_2$ into renewable fuel over Pt-g-$C_3N_4$/$KNbO_3$ composite photocatalyst. *RSC Adv.* **2015**, *5*, 93615–93622. [CrossRef]

98. Yu, H.J.; Li, J.Y.; Zhang, Y.H.; Yang, S.Q.; Han, K.; Dong, F.; Ma, T.Y.; Huang, H.W. Three-in-One Oxygen Vacancies: Whole Visible-Spectrum Absorption, Efficient Charge Separation, and Surface Site Activation for Robust $CO_2$ Photoreduction. *Angew. Chem. Int. Ed.* **2019**, *58*, 3880–3884. [CrossRef]

99. Yang, X.Y.; Min, Y.X.; Li, S.B.; Wang, D.W.; Mei, Z.W.; Liang, J.; Pan, F. Conductive Nb-doped $TiO_2$ thin films with whole visible absorption to degrade pollutants. *Catal. Sci. Technol.* **2018**, *8*, 1357–1365. [CrossRef]

100. Mattsson, A.; Leideborg, M.; Larsson, K.; Westing, G.; Österlund, L. Adsorption and solar light decomposition of acetone on anatase $TiO_2$ and niobium doped $TiO_2$ thin films. *J. Phys. Chem. B* **2006**, *110*, 1210–1220. [CrossRef]

101. Yang, J.K.; Zhang, X.T.; Wang, C.H.; Sun, P.P.; Wang, L.L.; Xia, B.; Liu, Y.C. Solar photocatalytic activities of porous Nb-doped $TiO_2$ microspheres prepared by ultrasonic spray pyrolysis. *Solid State Sci.* **2012**, *14*, 139–144. [CrossRef]

102. Nogueira, M.V.; Lustosa, G.M.M.M.; Kobayakawa, Y.; Kogler, W.; Ruiz, M.; Monteiro Filho, E.S.; Zaghete, M.A.; Perazolli, L.A. Nb-Doped $TiO_2$ Photocatalysts Used to Reduction of $CO_2$ to Methanol. *Adv. Mater. Sci. Eng.* **2018**, *2018*, 7326240. [CrossRef]

103. Thanh Truc, N.T.; Giang Bach, L.; Thi Hanh, N.; Pham, T.D.; Thi Phuong Le Chi, N.; Tran, D.T.; Nguyen, M.V.; Nguyen, V.N. The superior photocatalytic activity of Nb doped $TiO_2$/g-$C_3N_4$ direct Z-scheme system for efficient conversion of $CO_2$ into valuable fuels. *J. Colloid Interface Sci.* **2019**, *540*, 1–8. [CrossRef]

104. Faustino, L.A.; Souza, B.L.; Nunes, B.N.; Duong, A.T.; Sieland, F.; Bahnemann, D.W.; Patrocinio, A.O.T. Photocatalytic $CO_2$ Reduction by Re(I) Polypyridyl Complexes Immobilized on Niobates Nanoscrolls. *ACS Sustain. Chem. Eng.* **2018**, *6*, 6073–6083. [CrossRef]